NASA Technical Memorandum 88361

Interaction Between a Vortex and a Turbulent Boundary Layer

Part I: Mean Flow Evolution and Turbulence Properties

Russell V. Westphal, Wayne R. Pauley, and John K. Eaton

January 1987

National Aeronautics and Space Administration

NASA Technical Memorandum 88361

Interaction Between a Vortex and a Turbulent Boundary Layer
Part I: Mean Flow Evolution and Turbulence Properties

Russell V. Westphal, Ames Research Center, Moffett Field, California
Wayne R. Pauley,
John K. Eaton, Stanford University, Stanford, California

January 1987

National Aeronautics and
Space Administration

Ames Research Center
Moffett Field, California 94035

SYMBOLS

A_i, B_i, C_i, Di	five-hole probe calibration constants (see Appendix)
C_f	skin friction coefficient, $C_f = \tau_{wall}/(1/2\rho U_0^2)$
C_P	pressure coefficient, $C_P = (P(X) - P_0)/(1/2\rho U_0^2)$
$C_{P_{...}}$	five-hole probe pressure coefficients (see Appendix)
f_i	five-hole calibration functions (see Appendix)
h, l	vortex generator height and root chord, respectively
P	static pressure (measured with a wall static tap)
q^2	twice the turbulence kinetic energy, $q^2 = \overline{u'^2} + \overline{v'^2} + \overline{w'^2}$
R_Y, R_Z	vortex core vertical and spanwise directions radial dimensions
R_Γ	vortex circulation Reynolds number, $R_\Gamma = \Gamma/\nu$
u, v, w	velocity components in X, Y, Z directions
U, V, W	mean velocities; shorthand notation for $\overline{u}, \overline{v}, \overline{w}$
X, Y, Z	right-hand Cartesian coordinate directions
α	vortex generator angle-of-attack; also five-hole probe pitch angle
β	yaw angle for five-hole probe.
Γ	overall circulation of the main vortex
δ_{99}	boundary layer thickness, defined as $Y(U/U_e = 0.99)$
ν	air kinematic viscosity
ρ	air density
τ_{wall}	skin friction
ω_X	streamwise vorticity, $\omega_X = \partial W/\partial Y - \partial V/\partial Z$
$()_0$	reference value (measured at X=10 cm)
$()_C$	refers to vortex center
$()_e$	refers to local freestream conditions
$()_{max}$	maximum value for a particular crossflow plane
$\overline{()}$	(overbar) time average
$()'$	(prime) turbulence component, e.g.., $u = U + u'$

INTERACTION BETWEEN A VORTEX AND A TURBULENT BOUNDARY LAYER - PART 1: MEAN FLOW EVOLUTION AND TURBULENCE PROPERTIES

Russell V. Westphal, Wayne R. Pauley,[1] and John K. Eaton[1]

Ames Research Center

1. SUMMARY

The weakly three-dimensional (3-D) turbulent flow resulting from an interaction between a single streamwise vortex and a turbulent boundary layer has been investigated. Experiments have been performed in a low-speed wind tunnel for several cases with zero pressure gradient, and for one case with a moderate adverse pressure gradient. The vortex was generated using a half-delta wing mounted on the boundary layer test surface. Mean velocity, Reynolds stress, and skin friction measurements were obtained and analyzed.

A procedure was developed for quantitative characterization of vortex properties based on detailed measurements of the mean cross-flow velocity components. The procedure gave an objective, easily implemented means to define the vortex core position, size, and strength. Attenuation of core vorticity and a flattening of the core shape were studied; an accentuation of these effects was observed for the case with a moderate adverse pressure gradient. The question of whether the observed flattening was simply due to a quasi-steady motion of a round vortex - vortex *meander* - was examined using the mean velocity and turbulence measurements.

Turbulence properties were even more strongly perturbed in the case of adverse pressure gradient compared to the constant-pressure case. A substantial quantity of turbulence stress data are presented in the form of contour plots for comparison with computations of this flowfield. The further analysis and discussion of the implications of the present results for the purposes of turbulence model evaluation is to be included in a second (Part 2) report.

2. INTRODUCTION

Streamwise vortices often interact with turbulent shear layers in engineering systems; examples include the interaction of a strake-generated vortex with the main wing boundary layer on modern fighter aircraft configurations, and the tip vortex of one helicopter blade

[1]Stanford University, Stanford, CA.

impinging on a trailing blade. Another application of importance is the use of vortex generators to prevent or delay stall (separation) on airfoils or in diffusers. In all these applications, a vortex or array of vortices can interact with a turbulent boundary layer in the presence of a severe adverse pressure gradient. The combined effect of boundary layer turbulence and an adverse pressure gradient on a longitudinal vortex has not been investigated previously. The overall aim of the present research was to investigate the development of a fairly weak streamwise vortex embedded within a turbulent boundary layer in the presence of a moderate adverse pressure gradient.

There is considerable evidence that *strong* adverse pressure gradient alone can have a catastrophic effect on a discrete, free vortex. Batchelor (ref. 1) has considered changes in the structure of an axisymmetric, Rankine vortex caused by changes in streamwise velocity. His theoretical analysis indicates that, depending on the relative vortex strength, deceleration of the external stream beyond a certain critical value cannot occur without a total change in the structure of the vortex core. Vortices generated by a delta wing have been experimentally observed to undergo severe structural changes (ref. 2); it has been postulated that this *vortex breakdown* may be due to the effect of a strong adverse streamwise pressure gradient on the leading-edge vortex (refs. 2,3). It was also found experimentally that a very strong adverse pressure gradient was required to produce much affect on the particular free vortex configuration studied by Leuchter and Solignac, reference 3.

A substantial literature exists concerning the general features of the interaction between a vortex (or array of vortices) and a turbulent boundary layer. Much of the work concerns qualitative or first-order effects, such as tests to optimize vortex generators for stall prevention (refs. 4,5,6,7,8), examination of the drag created by vortex generators (refs. 9,10), the ubiquitous presence of vortices in wind tunnel boundary layer flows (refs. 11,12,13), and heat transfer beneath a vortex (ref. 14).

A few detailed studies of a vortex (or array of vortices) interacting with a turbulent boundary layer have been made. Shabaka et al., reference 15 (see also Mehta et al., reference 16) have studied single, weak vortices just above and later embedded within - the boundary layer in a constant-pressure flow. Their results showed a strong distortion of the distributions of the turbulence stresses within the boundary layer, in spite of the fact that the mean flow was only weakly three-dimensional. Takagi and Sato, reference 17, have examined the mean flow and turbulence properties of a vortex array interacting with a boundary layer. None of these studies addressed the issue of the *effect of the boundary layer on the vortex*, nor did they include the effects of an adverse pressure gradient.

Several studies (refs. 3,18,19,20) have indicated that *free* vortices at constant pressure evolve very slowly with streamwise distance. It is not expected that vortex behavior near a wall would be similar to that observed for a free vortex, because of the combined influence of boundary layer turbulence and the impermeability constraint (*image vortex*) imposed by the wall. The additional influence of an adverse pressure gradient would cause rapid

growth and increased turbulence stresses within the boundary layer and, therefore, would also be expected to affect vortex development. The existing literature contains very little information concerning the effect of a boundary layer on a vortex, and we have seen no work which demonstrates the additional effect of adverse pressure gradient on the interaction. The current specific research objective was to characterize a vortex as it interacts with the turbulent boundary layer with and without an adverse pressure gradient.

The contributions of Mr. Charles Hooper are gratefully acknowledged for writing some of the necessary data acquisition and reduction software. The authors would like to thank Dr. Rabi Mehta for many useful discussions which have contributed to the research. Review comments from Dr. Morris Rubesin are also gratefully acknowledged. Funds for the support of this study have been allocated by the NASA-Ames Research Center, Moffett Field. California, under Joint Research Interchange Numbers NCA2-1R745-405 and NCA2-18.

3. EXPERIMENTAL APPARATUS AND TECHNIQUES

The experiments were carried out in the Boundary Layer Wind Tunnel of the Fluid Dynamics Research Branch at NASA Ames Research Center (see fig. 1). This facility has a test section with dimensions of 20 by 80 by 300 cm and inlet freestream turbulence level of less than 0.2%. Inlet mean velocity uniformity at test speeds of 20-30 m/s was within 1% across the center half-span of the tunnel. A round wire trip (diameter 0.4 mm) was positioned at $X = 20$ cm on the test surface. The facility had an adjustable wall, opposite the flat test plate, for pressure-gradient control and probe access through slots.

A single vortex was generated with a half-delta wing mounted on the flat test surface (fig. 2). Different values of generator height, angle-of-attack, and streamwise position were employed as recorded in table 1. The generator heights used were chosen to position the vortex center near the undisturbed boundary layer edge at the station $X = 150$ cm. The non-dimensional vortex circulation obtained using these generators was about $\Gamma/lU_0 = 0.1 - 0.15$ when normalized on inlet freestream velocity U_0 and generator root chord l. The resulting vortex Reynolds number Re_Γ for all cases was approximately 10^4. The present study was purposefully designed to yield parameters for vortex and boundary layer properties similar to those used in the Imperial College experiments (refs. 15,16) (see table 2).

The present set-up differs from that used in the Imperial College work in the placement of the vortex generators. We elected to place the generator within the test section instead of in the settling chamber because this approach (1) made it easier to change the generator parameters, (2) caused no complex perturbation to the boundary layer until *after* tripping. thus giving a cleaner inlet condition, and (3) more accurately models the practical situation of vortex generators used on aircraft wings for stall control. The advantage of placing the generator within the settling chamber is that the wake defect is reduced on passage through

the contraction. It was concern over the generator wake which prompted the Imperial College workers to place the generator in the wind tunnel contraction (ref. 15), and to assert that some undesirable effects may accrue because of the wake (ref. 21). Thus, the possible effects of the wake on the details of the interaction are of interest in comparing the present and previous results, and this question will be examined as the results are presented below.

Three-component mean velocity measurements were made using four different multihole pressure probes with configurations as summarized in table 3. The four-hole probe (F) was the same as used by Youssefmir, reference 22, and we employed his published response equations and calibration. Three different five-hole pressure probes were also used for the experiments, with the smaller probes employed where improved spatial resolution was required, such as for measurements nearest the vortex generator. Further downstream, spatial resolution requirements were relaxed because of enlargement of the vortex core and boundary layer growth. Calibration of the five-hole probes was obtained using a simplification of the method outlined by Treaster and Yocum, reference 23, further described in the Appendix.

Early in the work, it was observed that the multihole probes gave an apparent velocity component which was caused by local velocity gradient. For instance, a five-hole probe placed within a boundary layer will read a lower pressure on the tap nearer the wall than on the tap farthest from the wall; this can be erroneously interpreted as a velocity vector pitched toward the wall. Depending on the probe size and on the local velocity gradients (i.e., position in the flow), this error can be quite substantial.

The effect of local velocity gradient on the multihole probe data was quantified, and a gradient correction algorithm selected, based on measurements in the boundary layer without the vortex. The procedure adopted was to simply subtract an apparent component attributable to velocity gradient from the measured V and W components. Since the vortex flow is only weakly 3-D, the apparent component was estimated to be a constant (a function only of the probe geometry) multiplied by the local gradient of velocity magnitude. The velocity gradient was obtained by analytic evaluation of derivatives from a cubic spline interpolation of the measured data. The correction length scale selected was approximately equal to the separation between the off-center pressure taps for each probe, and the same gradient-correction length scale was applied in both the spanwise (Z) and vertical (Y) directions. Including calibration uncertainties and after correction for velocity gradient effects, the uncertainty in velocity measurements with the five-hole probe are estimated at less than 1.5% for the velocity magnitude and 0.3° for *variations* in flow angle within a particular streamwise plane. There remains an additional uncertainty of about 0.5° in measurement of the absolute reference flow angle relative to, say, the plane of the test surface; however, this uncertainty does not influence determination of the vorticity.

Measurements of all three components of mean velocity and five of the six independent components of the Reynolds stress tensor were obtained using an automated crossed hot-wire anemometer system. The probe was rolled about its axis to obtain both $X - Y$ and

$X - Z$ plane measurements; our procedure did not allow for measurement of the cross-flow plane Reynolds shear stress component $\overline{v'w'}$. The probe's 5 μm diameter tungsten sensor wires were about 1 mm in length and spaced 1 mm apart, and were operated with 80% overheat. Possible effects caused by finite probe measurement volume have been neglected for the present work; note that the X-wire dimensions are substantially smaller than the multihole probes described above. Calibration was repeated every four hours, and flow temperature was held constant to within 1 C during these runs. Response equations and calibration procedures used are outlined in reference 24. Because two measurement planes were required, and considering the time-consuming X-wire calibrations, the multihole probe was preferred over the X-wire for measurements of mean velocity only, and for initial scans used to select run conditions for detailed hot-wire traverses.

Skin friction was measured and visualized beneath the vortex using the oil film interferometry technique (refs. 25,26). A special test plate with a partially reflective metal-coated glass insert was employed for the latter work. Silicone oil of nominal viscosity 50 cS was used. A round Preston tube of outside diameter 0.71 mm was also used for skin friction measurements; Patel's calibration (ref. 27) was adopted for this work.

A PDP-11/44 minicomputer with two 10 MB hard disk drives and 256 kB of memory was used for data acquisition. The software employed for instrument calibration, database management, graphics, and data acquisition is described in two reports (refs. 28,29).

4. RESULTS AND DISCUSSION

Selected results from the experiments are presented below. First, the experimental test conditions are outlined. Next, procedures used for characterizing the vortex properties are described, then the vortex properties are shown for the various experiments. In a separate section, a detailed discussion of the streamwise evolution of the mean flow and turbulence measurements for one case is presented with selected data from other cases included to demonstrate the effects of adverse pressure gradient and generator configuration. The final section gives a discussion of evidence related to vortex *meander*. Although no tabular data are included, these data can be provided to the interested reader by arrangement with the first author (RVW).

4.1 Test Conditions

Two test conditions were selected: one case with nominally zero pressure gradient, and a second case with adverse pressure gradient. For the former, the control wall was adjusted for constant pressure coefficient, C_P, within 0.5% over the entire test section ($0 < X < 300$ cm). For the adverse pressure gradient case, the control wall was adjusted to give a moderate

adverse pressure gradient, followed by a region of recovery at constant pressure. Figure 3 shows the measured pressure distributions for these cases. Note that the inlet velocity, U_0, was used to normalize all quantities in the presentation of data. It proved convenient to use slightly different values of U_0 (24.5 – 27 m/s) for the various experiments; for any particular experiment, U_0 was continuously monitored and maintained constant to within 0.5%.

The thickness of the boundary layers without the vortex for each case is tabulated below.

	X cm		
δ_{99} cm	100	200	300
A (constant pressure)	1.4	2.8	4.0
B (adverse gradient)	1.7	4.3	6.2

Taken together, the vortex generator configuration and the wind tunnel set-up comprise a complete specification of experimental conditions. For example, case A3 indicates the constant-pressure boundary layer with vortex generator configuration number 3. These designations are used below to describe each case.

4.2 Definition of Vortex Scalar Descriptors

A key to quantifying vortex evolution was to establish appropriate parameters to characterize the size and strength of a vortex. Because of the effect of a nearby solid surface in producing an image vortex, cross-flow velocity vectors alone cannot be easily interpreted – it is only for an *isolated* vortex that the velocity field may be directly interpreted to yield vortex core position and strength. Calculation of streamwise mean vorticity from the measured cross-flow velocity components provided the means for characterizing the vortices, as discussed in reference 30. Briefly, natural cubic splines were used to interpolate the measured distributions of V and W in a particular measurement plane. Then the spatial derivatives of V and W needed to compute ω_X were evaluated analytically from the interpolation functions. This same procedure for computation of vorticity from point-wise measurements was recently reported by Brune and Hallstaff, reference 31, for analysis of data in the wake of a lifting wing. Finite-difference representations for the spatial derivatives have also been used, and give about the same results with the present fine measurement grid. Scalars describing the vortex were extracted from the vorticity distributions, as explained below.

The vortex position was easily located as the geometric center of the concentric vorticity contours. Vortex core strength was characterized by the peak value of vorticity attained in the core, $\omega_{X,max}$. Overall circulation Γ was simply defined as the integral of the vorticity over the cross-flow plane; to provide some noise immunity in performing this integration, vorticity levels less than 10% of the peak were neglected. In a few cases, the vorticity integrals were compared to line integrals of the crossflow velocity field taken outside the 10% contours:

the circulation values obtained by these two methods generally agreed within 10% (which improved confidence in the method of computing the vorticity).

Because elliptical vorticity contours were observed further downstream in some cases, vortex size had to be defined using two length scales. These were chosen as the vertical and spanwise radial dimensions measured from the vortex center where the vorticity had decreased to 50% of the peak value of $\omega_{X,max}$. Other contours may be used equally well to define the vortex core length scale, but values less than 30% of the peak are probably within the resolution in determination of vorticity, particularly in regions where the peak vorticity levels have fallen by more than an order of magnitude from their initial levels. Generally, the 20% contour radius was about 40% larger than the value from the 50% contour.

Uncertainty in the determination of vorticity ω_X controls the uncertainty in determination of vortex dimensions and overall circulation. The uncertainty in values of ω_X/U_0 determined in the present study was estimated at 10% of the value, plus an additional (constant) uncertainty of 0.01 cm^{-1} representing the minimum resolvable value. Thus, uncertianties in the quantities derived from the computed vorticity are smallest ($\sim$ 10%) when the vorticity levels are large, and rise as the peak vorticity decreases farther downstream. At the furthest downstream stations, uncertainties rise to over 25% for the peak vorticity, and cause concomitant increases in the percentage uncertainties in vortex dimensions and overall circulation estimates. This fact must be borne in mind when interpreting the results.

In summary, four scalar descriptors of vortex properties have been identified. These are (1) vortex core center position (Y_C, Z_C), (2) peak vorticity $\omega_{X,max}$, (3) overall circulation Γ/ν, and (4) vortex core dimensions (R_Y, R_Z). The streamwise development of these vortex properties is discussed in the next section.

4.3 Streamwise Development of Vortex Properties

Figure 4 depicts the vertical and spanwise displacement of the vortex center as a function of streamwise position. The vortex moves slightly away from the wall, following approximately the growth in boundary layer displacement thickness. The observed spanwise displacement of the core in the negative Z direction was attributable to the velocity induced by the image vortex at the vortex core center position. The total induced spanwise displacement caused at the vortex center by its image, over a distance $\Delta(X)$, is given approximately by the relation $\Delta(Z_c)/\Delta(X) = \Gamma/(4\pi Y_C U_C)$. From the data for case A1, for example, the values of $\Gamma/U_0 = 0.5$ cm, $U_C/U_0 = 0.9$, and $Y_C = 1.7$ cm give an estimated rate of spanwise motion of $\Delta(Z_C)/\Delta(X) = 0.026$. This compares closely to the actual measured value of 5 cm spanwise motion between $X = 115$ and $X = 298$ cm, which yields a value of 0.027.

The overall circulation of the vortex, Γ/U_0, was observed to decrease slowly or remain about constant over the length of the test section as shown in figure 5 for the various cases.

Peak vorticity $\omega_{X,max}/U_0$ decreased about an order of magnitude over the same distance (see fig. 6). The strong attenuation in peak core vorticity is accompanied by rapid growth of the vortex core. Figure 7 shows the vertical and spanwise core radii R_Y and R_Z, respectively; it is noted that the vertical growth rate of the core decreases with X, while the spanwise dimension grows steadily, indicating that the vortex core is beginning to flatten.

Comparing the data of figures 6 and 7 from all three constant constant-pressure cases to the case of adverse gradient (Case B1), it is noted that the pressure gradient causes a more rapid attenuation of the peak vorticity, accompanied by accelerated core growth. The increased vortex core growth is only partially accounted for by Batchelor's (ref. 1) simple model for core growth caused solely by changes in streamwise velocity in the far-field. Using our values for vortex diameter and circulation yields a nondimensional vortex strength ka^2 of less than 0.3, and solution of equation (7.5.25) of reference 1 with a value of the velocity ratio of 0.73 yields a core growth of 18%. This is in contrast to the experimental results, which indicated that the vortex core affected by adverse pressure gradient was some 50% greater in diameter than the constant-pressure case by the end of the test section.

The flattening of the vortex core was quantified by computing the ellipticity of the 50% contour, defined as R_Z/R_Y, shown in figure 8. The flattening appears to begin abruptly and this, in turn, appears to be associated with the growth of the vertical dimension of the vortex core. If the data for core position and vertical dimension are combined to form the nondimensional core position R_Y/Y_C, it is noted (fig. 9) that core growth in the vertical direction ceases at a value of $R_Y/Y_C \sim 0.5$. This observation is more clearly presented by cross-plotting the ellipticity ratio R_Z/R_Y as a function of the nondimensional core position R_Y/Y_C as shown in figure 10 for all four cases. Thus, we observed that the vortex within a boundary layer displays a very rapid reduction of its core vorticity, and a flattening of the core shape when the vertical dimension R_Y reached a critical value of about $R_Y \sim 0.5Y_C$.

The adverse pressure gradient was observed to cause a striking increase in the amount of core flattening, as clearly shown by figure 8. An ellipticity ratio of nearly 3 was obtained for the adverse gradient case, compared with a value of about 2 for the constant-pressure cases. It appears that the main effect of adverse pressure gradient - an increased rate of core growth - caused the flattening to develop sooner and become more pronounced.

4.4 Details of Streamwise Flow Development

Because the flow under study was three-dimensional and turbulent, a tremendous amount of data were generated. For example, at a typical plane in the flow, measurements were made at 400-700 locations. At each location, in the case of X-wire data, three mean velocity components and five Reynolds stresses were recorded. As many as ten data planes were

[2]Batchelor's ka is roughly equivalent to $\Gamma/\pi U_0 R$

obtained for each of the cases studied, including three constant-pressure cases and one case with an adverse pressure gradient. Thus, to reduce the amount of data to be presented while still conveying the important details of flow evolution, only results from case A3 will be covered in detail. Highlights from the other cases will be presented to demonstrate the effects of varying the vortex generation parameters and the effects of adverse pressure gradient.

4.4.1 Mean velocity, vorticity, and skin friction. The streamwise mean velocity distribution within the boundary layer is strongly distorted by the presence of the vortex. Figure 11 shows contours of mean streamwise velocity U/U_0 at several streamwise stations; the boundary layer is effectively thickened on the upwash side, and thinned in the downwash region of the vortex. The contour shapes at the various downstream stations are quite similar, explaining again why this flow has been termed *slowly evolving.*

The wake of the generator is visible as a symmetrical mean velocity defect in the contours of U/U_0 at the more upstream locations. Figure 12 shows that the wake effects are less for generators with a smaller angle-of-attack, as would be expected. However, the three different generator configurations produced little variation in the evolution of the vortex properties, as demonstrated by comparison of results for cases A1, A2, and A3 in figure 9. The apparent insensitivity to varying generator placement and geometry is evidence that the generator wake has very little effect on the interaction between a vortex and a boundary layer.

Cross-flow plane velocity vectors are shown for several streamwise locations in figure 13. These vector plots demonstrate the importance of the image flow in producing the observed cross-flow patterns; for example, the velocities observed beneath the vortex are much larger than those above the vortex. From these patterns alone, it would not be easy to consistently define vortex scalar properties because of the image effects. However, by plotting *vorticity* ω_X computed from these data, the confusing influence of the image can be eliminated. Figure 14 shows the vorticity distributions corresponding to the velocity vectors shown in figure 13. The scalar descriptors obtained from these contours were presented in the preceeding section.

The data of figure 13 indicates that surface flow angles should be small, even directly beneath the vortex. Thus, no attempt has been made to separately measure the spanwise component of skin friction. However, it was not known whether Preston tube measurements could be trusted, because the use of Patel's calibration relies upon near-wall flowfield similarity with the classic turbulent boundary layer. *Direct* measurements made using the oil film interferometer at one location were compared to the Preston tube data to check this basic assumption. The results, shown in figure 15, indicate that the Preston tube results are generally reliable, although the indicated peak values may be somewhat low. The implication is that near-wall flowfield similarity is generally satisfied for this weakly 3-D flow, a conclusion which is also supported by the results of reference 14, where surface fence data were compared with results inferred from assuming the usual log-law similarity of velocity profiles.

Figure 16 shows Preston tube skin-friction measurements at successive streamwise locations. As observed from previous measurements (refs. 10,14,15,16), there is a large variation of skin friction beneath the vortex, with peak values more than twice the minimum. The peak C_f value decreases rapidly downstream, whereas the minimum value varies little. The apparent spanwise shift in the distributions is caused by the displacement of the vortex core center as explained above.

4.4.2 Turbulence properties. Figure 17 shows the contours of the turbulence kinetic energy q^2/U_0^2 at successive streamwise locations for Case A3. These contours appeared quite similar to the pattern of the mean streamwise velocity contours, indicating that the turbulence energy is distributed approximately as if the flow were locally 2-D. The contours near the vortex generator displayed peaks in q^2/U_0^2 within the vortex core which were due to the persistence of the generator wake for this case. Little qualitative difference was noted among the behavior of the three individual normal stress components $\overline{u'^2}/U_0^2$, $\overline{v'^2}/U_0^2$, and $\overline{w'^2}/U_0^2$, as evidenced by the data shown in figure 18 (note the different contour levels in these figures), although the local anisotropy in the Reynolds stresses is an interesting feature of the *vortex core* flow.

Strongly disturbed distributions of the primary Reynolds shear stress $\overline{u'v'}/U_0^2$, shown in figure 19, measured in the presence of the vortex are in general agreement with those shown in previous work (refs. 15,17). Note that a region of small and even locally positive correlation of u' and v' is generally observed within the region around the core, where strongly disturbed distributions of the *normal* gradient of mean streamwise velocity were noted.

Another component of the turbulence shear stress, $\overline{u'w'}/U_0^2$, is shown in figure 20. Maximum and minimum values of this quantity were observed in the upwash region, and were qualitatively correlated with regions of maximum *spanwise* gradients in mean streamwise velocity. In previous work (ref. 15), larger values of $\overline{u'w'}/U_0^2$ were measured away from the upwash region than were found in the present work; at this time, no explanation of this discrepancy is apparent.

Application of moderate adverse pressure gradient caused no major qualitative changes in the turbulence stress distributions. Figure 21(a-c) shows contours of turbulence kinetic energy and the two measured turbulence shear stresses at one streamwise station for the adverse pressure gradient case. The main effect of adverse pressure gradient was to cause higher levels of turbulence stresses farther from the surface within the boundary layer – the combined effect of the vortex and adverse pressure gradient caused a more severe distortion of the boundary layer Reynolds stresses.

The turbulence measurements provide further evidence that the vortex generator wake has little effect on the main features of the interaction. As the wake decayed, the peak in q^2/U_0^2 disappeared (fig. 17), but no change in the general shape of the distributions of the critical Reynolds shear stress components $\overline{u'v'}$ and $\overline{u'w'}$ was observed. Thus, the presence

and decay of the weak generator wake appears to be uncoupled from the interaction itself, and does not assert a complicating influence.

4.5 Evidence Related to Vortex *Meander*

It has been suggested that a vortex near a solid wall tends to move side-to-side along the surface in a quasi-steady manner; this motion has been termed *meander*. The fact that the mean vorticity is initially strongly concentrated within a small *round* core strongly suggests that the vortex does not display meander at upstream locations (near the vortex generator). Thus, the suggestion (ref. 32) that meander is an inherent feature of wall-bounded flows with discrete vortices is not supported by the present results in regions where the vorticity contours are round. The existence of sharp minima and maxima in the spanwise skin friction distributions (refer to figs. 15 and 16) also suggests that the vortex does not meander. Since the sharpness of the distributions – particularly the minima – does not change much with streamwise position, it appears that no appreciable meander occurs at any position.

Further downstream of the generator, a flattening of the vortex core shape was observed (cf. figs. 8 and 14). It was initially believed that this might be evidence that the vortex was meandering; however, results for the spanwise component of the normal Reynolds stress $\overline{w'^2}$ suggest that the vortex does not meander. For example, a side-to-side motion of the vortex should show up directly as increased levels of $\overline{w'^2}$, but the values of this component were found to be similar to the upstream values. And, production of $\overline{u'w'}$ would accrue from meander due to the action of the mean strain dU/dZ with the term $\overline{w'^2}$, but again no significant differences were noted in the contours of $\overline{u'w'}$ when the contours of mean vorticity were circular compared to when these contours became more elliptic (see fig. 20).

Estimates of the likely increase in measured turbulence stresses caused by meander, also called *apparent* stresses, indicated that the apparent stresses may be very small at downstream locations. For example, using the data for case A1 at $X = 200$ cm and an amplitude of 1 cm for the meander, apparent values of $\overline{u'w'}$ from local $\partial U/\partial Z$ and apparent $\overline{w'^2}$ were estimated to be barely measureable. Thus, the evidence cited above was considered inconclusive regarding possible meander at locations where vortex core flattening was evident, and additional work is underway to examine this question more fully.[3]

5. CONCLUSIONS

An interaction between a turbulent boundary layer and a relatively weak embedded streamwise vortex has been investigated experimentally, including the effects of adverse

[3] Westphal, R. V. and Mehta, R. D.; Meander of a Vortex in a Turbulent Boundary Layer. in progress, 1987.

streamwise pressure gradient. The most interesting results concern the effects of the boundary layer on the vortex properties.

Contours of streamwise vorticity computed from the mean crossflow velocity distribution were used to characterize the vortex. Substantial vortex core growth was observed for both constant pressure conditions and for the case of moderate adverse gradient compared to that which would have been expected for a similar free vortex. Accelerated core growth was noted caused by the adverse pressure gradient; the increase in core growth over that found for the constant-pressure case was not fully accounted for by Batchelor's simple theory.

When the vortex core radius grew to a sufficient fraction of the height of the vortex center from the wall, the vorticity contours became increasingly elliptic in shape. The onset of ellipticity was accelerated in the case of adverse pressure gradient caused by the higher core growth rate. The vorticity contours were initially found to be round, suggesting that the vortex does not meander near the generator. Further downstream, the hypothesis that the apparent ellipticity of the vortex was really a manifestation of meander was tested by examination of the turbulence measurements. There was no evidence of meander in these data, but this evidence was inconclusive because the apparent stresses caused by meander were estimated to be only barely measureable.

The use of a generator mounted on the boundary layer test plate caused a decaying wake to be present in these experiments. However, it was found that the wake obtained from the particular configuration used (half-delta wing at small angle-of-attack) had little effect on the observed features of the interaction, and should not produce objectionable complications.

The general features of the turbulence stress distributions were mostly similar to those reported by previous investigators for the case of no streamwise pressure gradient. Overall, distortion of the Reynolds stresses was more pronounced in the case of adverse pressure gradient compared to flat-wall boundary layer values. Thus, challenges to turbulence modeling even greater than for the constant pressure case are anticipated because of the larger regions of strongly disturbed stress levels. The turbulence data and modeling considerations are discussed in a companion report.[4]

[4] Westphal, R. V.; *Interaction Between a Vortex and a Turbulent Boundary Layer - Part 2: Turbulence Data Analysis and Discussion.* NASA TM, in progress, 1987.

APPENDIX: FIVE-HOLE PRESSURE PROBE RESPONSE EQUATIONS

Following Treaster and Yocum, reference 23, (hereafter TY), four nondimensional pressure coefficients are defined in terms of the measured pressures from the five probe tappings. Figure 22 shows the coordinate system and hole numbering convention, which is identical to that used by TY. Both the original definitions of TY, using measured pressures P_i from each of the 5 tappings, and their equivalent forms using measured pressure *differences* $\Delta P_i = P_i - P_{ref}$ relative to an arbitrary (fixed) reference are given below. The forms using $\Delta P_i = P_i - P_{ref}$ are most convenient for use with automatic pressure scanning systems, such as that used for the present work.

$$C_{P,pitch} = \frac{P_4 - P_5}{P_1 - \overline{P}} = \frac{\Delta P_4 - \Delta P_5}{\Delta P_1 - \overline{\Delta P}}$$

$$C_{P,yaw} = \frac{P_2 - P_3}{P_1 - \overline{P}} = \frac{\Delta P_2 - \Delta P_3}{\Delta P_1 - \overline{\Delta P}}$$

$$C_{P,total} = \frac{P_1 - P_{total}}{P_1 - \overline{P}} = \frac{\Delta P_1 - (P_{total} - P_{ref})}{\Delta P_1 - \overline{\Delta P}}$$

$$C_{P,static} = \frac{\overline{P} - P_{static}}{P_1 - \overline{P}} = \frac{\overline{\Delta P} - (P_{static} - P_{ref})}{\Delta P_1 - \overline{\Delta P}}$$

For the above, $\overline{P}$ is defined as the average of the off-center pressures:

$$\overline{P} = \frac{(P_2 + P_3 + P_4 + P_5)}{4}$$

$$\overline{\Delta P} = \frac{(\Delta P_2 + \Delta P_3 + \Delta P_4 + \Delta P_5)}{4}$$

Note that the reference pressure selected for the measurement of pressures will not matter insofar as $C_{P,pitch}$ and $C_{P,yaw}$ are concerned. The functional form for the probe response used by TY is also adopted:

$$\alpha = f_1(C_{P,pitch}, C_{P,yaw})$$

$$\beta = f_2(C_{P,pitch}, C_{P,yaw})$$

$$C_{P,total} = f_3(\alpha, \beta)$$

$$C_{P,static} = f_4(\alpha, \beta)$$

TY used an interpolation of calibration data obtained over a range of pitch and yaw angles to represent the functions f_i. For application to the present case of small flow angle – within about 15° from the probe axis – we have simplified the probe response functions by assuming symmetry but no coupling between f_1 and f_2. These simplifications were suggested by inspection of data digitized from TY, which is shown in figures 23 and 24. These plots demonstrate that, for angles of pitch and yaw both within up to 20°, the uncoupled functions should be quite accurate. The representation actually employed for the present study was:

$$f_1(C_{P,pitch}) = (C_{P,pitch} - A_1)(A_2 - A_3|C_{P,pitch} - A_1|)$$

$$f_2(C_{P,yaw}) = (C_{P,yaw} - B_1)(B_2 - B_3|C_{P,yaw} - B_1|)$$

The parameters A_i and B_i were determined by a least-squares fit to calibration data. Note that since the small angle approximation uncouples the pitch and yaw functions, the calibration data need not include compound pitch and roll angles. Also, the choice of reference pressure is arbitrary insofar as determination of the flow angles is concerned since, as noted above, neither $C_{P,pitch}$ nor $C_{P,yaw}$ depend on the reference pressure used.

With the flow angle known, it remains to determine the velocity vector magnitude. Again, symmetry considerations along with the results of TY suggested a simple functional representation for f_3 and f_4:

$$f_3(\alpha, \beta) = C_1(1 - C_2\alpha^2)(1 - C_2\beta^2)$$

$$f_4(\alpha, \beta) = 1 - D_1(1 - D_2\alpha^2)(1 - D_2\beta^2)$$

For the present case, the static pressure variation at any cross-section of the flow was negligible; thus, we elected to treat the static pressure as known and adopted a procedure

of using the local wall static pressure as the reference for all pressure measurements. In this case, $C_{P,static}$ can be computed directly from only the measured data, so that only the parameters D_i are actually needed from calibration to allow calculation of $C_{P,total}$. Then the velocity magnitude $|\overline{V}|$ and vector components U, V, and W follow from the definitions of the pressure coefficients given above, using the TY conventions for flow angles as shown in figure 22.

$$|\overline{V}| = \sqrt{(\frac{2}{\rho})(\Delta P_1 - \overline{\Delta P})(1 + C_{P,static} - C_{P,total})}$$

$$U = |\overline{V}| \cos\alpha \cos\beta$$

$$V = |\overline{V}| \sin\alpha \cos\beta$$

$$W = |\overline{V}| \sin\beta$$

REFERENCES

1. Batchelor, G. K.: *Introduction to Fluid Dynamics.* Cambridge University Press, Cambridge, England, 1967.

2. Leibovich, S.: Vortex Breakdown and Stability: Survey and Extension. *AIAA Journal*, vol. 22, vo. 9, Sept. 1984, p. 1192.

3. Leuchter, O., and Solignac, J. L.: Experimental Investigation of the Turbulent Structure of Vortex Wakes. *Proceedings of the Fourth Symposium on Turbulent Shear Flows*, Karlsruhe, W. Germany, 1983, p. 5.31.

4. Schubauer, G. B., and Spangenberg, W. G.: Forced Mixing in Boundary Layers. *J. Fluid Mech.*, vol. 8, no. 1, 1960, p. 10.

5. Brown, A. C., Nawrocki, H. F., and Paley, P. N.: Subsonic Diffusers Designed Integrally with Vortex Generators. *J. Aircraft*, vol. 5, no. 3, May-June 1968, p. 221.

6. Spangler, J. G., and Wells, C. S. Jr.: *Effects of Spiral Longitudinal Vortices on Turbulent Boundary Layer Skin Friction.* NASA CR-145, Dec. 1964.

7. Stein, D. E.: Case History: Use of Vortex Generators in Aircraft Design. *Airliner*, no. 4, Oct.-Dec. 1985, p. 5.

8. McMasters, J. H., Crowder, J. P., and Robertson, P. E.: Recent Applications of Vortex Generators to Wind Turbine Airfoils. AIAA paper 85-5014, Oct. 1985.

9. Rao, D. M., and Mehrotra, S. C.: *Flat-Plate Drag Measurements with Vortex Generators in a Turbulent Boundary Layer.* NASA CR-172125, 1983.

10. Tanner, L. H., and Kulkarni, V. G.: The Viscosity Balance Method of Skin Friction Measurement: Further Developments including Applications to Three-Dimensional Flow. *J. Physics E.: Sci. Instrum.*, vol. 9, no. 12, Dec. 1976, p. 1114.

11. Morkovin, M. V.: *Observations on Streamwise Vortices in Laminar and Turbulent Boundary Layers.* NASA CR-159061, 1979.

12. Tani, I. (translated by K. Horiuti, 1985): Formation of Longitudinal Vortices in a Shear Flow. *J. Japan Soc. for Fluid Mech.*, vol. 2, no. 2, Feb. 1983, p. 160.

13. Mokhtari, S., and Bradshaw, P.: Longitudinal Vortices in Wind Tunnel Wall Boundary Layers. *Aero. J.*, vol. 87, June-July, 1983, p. 233.

14. Eibeck, P. A., and Eaton, J. K.: *An Experimental Investigation of the Heat Transfer Effects of a Longitudinal Vortex Embedded in a Turbulent Boundary Layer.* Report MD-48, Mechanical Engrg. Dept., Stanford Univ., Nov. 1985.

15. Shabaka, I. M. M. A., Mehta, R. D., and Bradshaw, P.: Longitudinal Vortices Imbedded in Turbulent Boundary Layers. Part I - Single Vortex. *J. Fluid Mech.*, vol. 155, no. 6, June 1985, p. 37.

16. Mehta, R. D., Shabaka, I. M. M. A., Shibl, A., and Bradshaw, P.: Longitudinal Vortices Imbedded in Turbulent Boundary Layers. AIAA paper 83-0378, Jan. 1983.

17. Takagi, S., and Sato, H. (in Japanese, not translated): An Experiment on the Interaction of a Turbulent Boundary Layer and a Row of Longitudinal Vortices. *J. Japan Soc. for Fluid Mech.*, vol. 2, no. 3, Mar. 1983, p. 288.

18. Hoffman, E. R., and Joubert, P. N.: Turbulent Line Vortices. *J. Fluid Mech.*, vol. 16, May-Aug. 1963, p. 395.

19. Phillips, W. R. C., and Graham, J. A. H.: Reynolds-Stress Measurements in a Turbulent Trailing Vortex. *J. Fluid Mech.*, vol. 147, Oct. 1984, p. 353.

20. Pearson, C. F., and Abernathy, F. H.: Evolution of the Flow Field Associated with a Streamwise Diffusing Vortex. *J. Fluid Mech.*, vol. 146, Sept. 1984, p. 271.

21. Cutler, A. D., and Bradshaw, P.: The Interaction Between a Strong Longitudinal Vortex and a Turbulent Boundary Layer. AIAA paper 86-1071, June 1986.

22. Youssefmir, P.: *Flow Studies of Full-Coverage Film Cooling on a Convexly Curved Surface.* Engineer's thesis, Stanford University, Oct. 1982.

23. Treaster, A. L., and Yocum, A. M.: The Calibration and Application of Five-Hole Probes. *ISA Trans.*, vol. 18, no. 3, Mar. 1979, p. 23.

24. Westphal, R. V., and Mehta, R. D.: *Crossed Hot-Wire Anemometry Data Acquisition and Reduction System.* NASA TM-85871, Jan. 1984.

25. Tanner, L. H.: The Application of Fizeau Interferometry of Oil Films to the Study of Surface Flow Phenomena. *Optics and Lasers in Engrg.*, vol. 2 no. 3, May-June, 1981, p. 105.

26. Westphal, R. V., Bachalo, W. D., and Houser, M. J.: *Improved Skin Friction Interferometer.* NASA TM-88216, Mar. 1986.

27. Patel, V. C.: Calibration of the Preston Tube and Limitations on its Use in Pressure Gradients. *J. Fluid Mech.*, vol. 23, Sept. 1965, p. 185.

28. Hooper, C., and Saunders, D.: *FMDAS: Fluid Mechanics Data Acquisition System.* Report 7104-307, no. 13, Informatics General Corp., Feb. 1985.

29. Lichtenstein, T., and Saunders, D.: *Data Management System for Mid-sized Data Acquisition and Display Systems.* Report 7104-307, no. 11, Informatics General Corp., Dec. 1983.

30. Westphal, R. V., Eaton, J. K., and Pauley, W. R.: Interaction Between a Vortex and a Turbulent Boundary Layer in a Streamwise Pressure Gradient. *Proceedings of the Fifth Symposium on Turbulent Shear Flows.* Ithaca, N. Y., 1985, p. 7.1.

31. Brune, G. W., and Hallstaff, T. H.: Wing Span Loads of Complex High-Lift Systems from Wake Measurements. *J. Aircraft*, vol. 22, no. 9, Sept. 1985, p. 831.

32. Bushnell, D. M.: Body-Turbulence Interaction. AIAA paper 83-1527, June 1983.

TABLE 1. - VORTEX GENERATORS USED.

Generator number	Position X cm	Root chord l cm	Angle-of-attack α deg.	Height h cm
1	90.	3.8	12	1.8
2	50.	3.8	12	1.8
3	50.	3.8	16	1.5

TABLE 2. - PARAMETERS OF THE EXPERIMENT.

Experiment:	Present	Imperial College 15,16
Test section dimensions, cm	20 x 80 x 300	13 x 76 x 290
Freestream speed U_0, m/s	24.5 - 27.0	30.0
Boundary layer trip and X location, cm	0.4 mm wire $X = 20$	1.0 mm wire $X = 0$
Vortex circulation Γ/U_0, cm	0.5	0.2
Vortex core height at X = 200 cm	1.7	2.5
Vortex generator location	on test surface	in wind tunnel settling chamber

TABLE 3. - CHARACTERISTICS OF THE FOUR MULTI-HOLE PROBES USED.

Probe	No. holes	Type[a]	Probe tip O.D. mm	Hole I.D. mm
F	4	f	3.0	0.5
S	5	f	1.8	0.15
M	5	f	2.3	0.25
L	5	c	3.5	0.5

[a]f:faceted, c:conical; both have 90° included tip angle

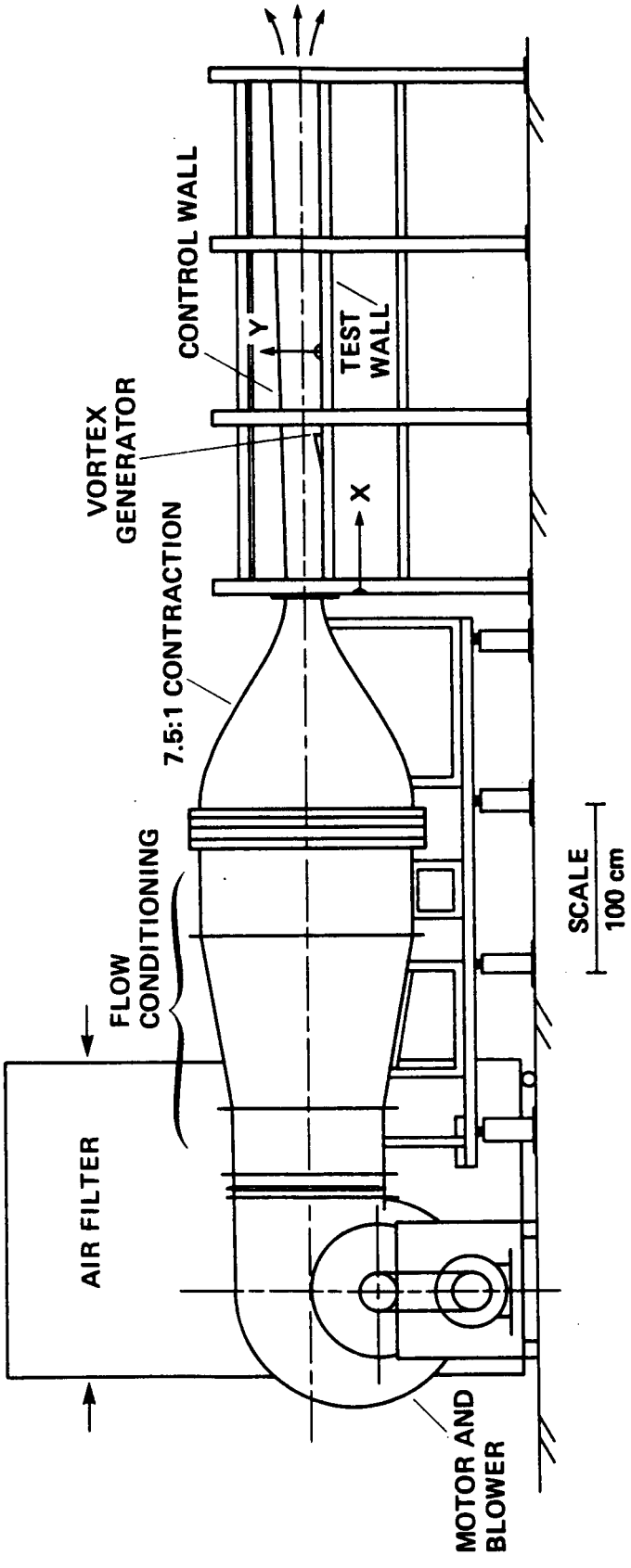

Figure 1. - Boundary layer wind tunnel schematic.

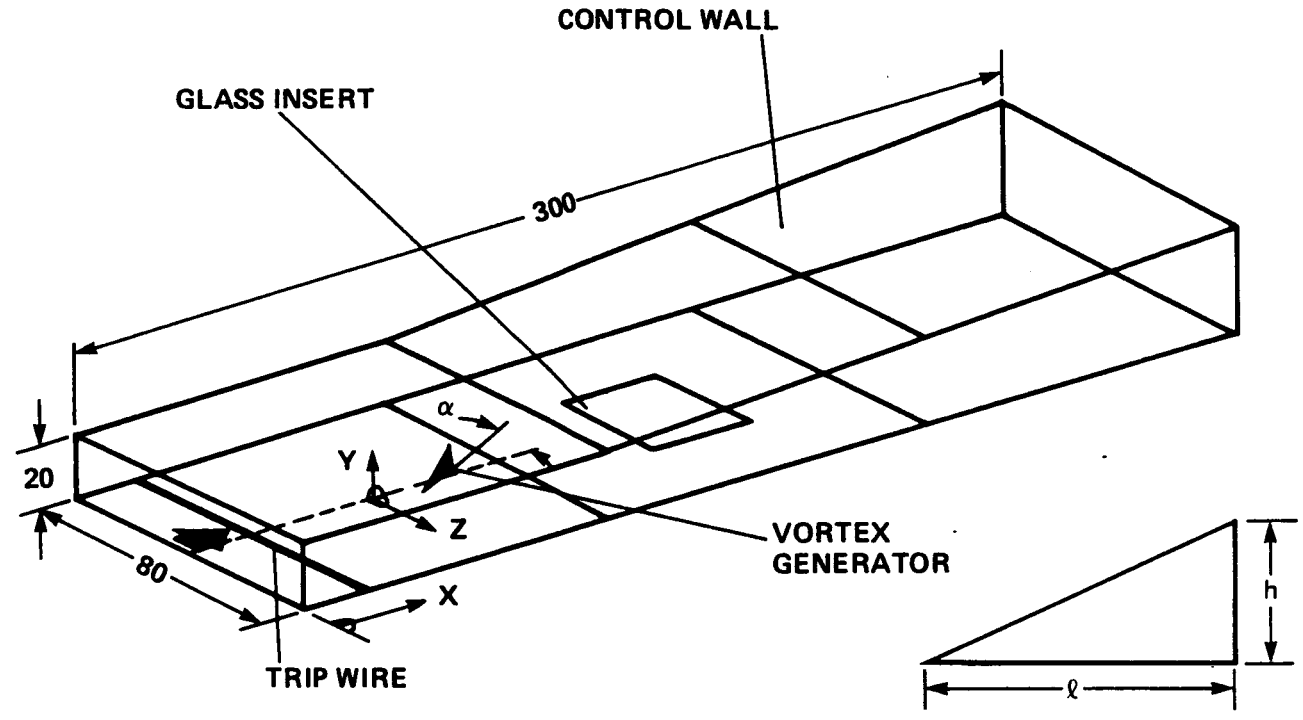

Figure 2. - Wind tunnel test section showing vortex generator geometry and positioning.

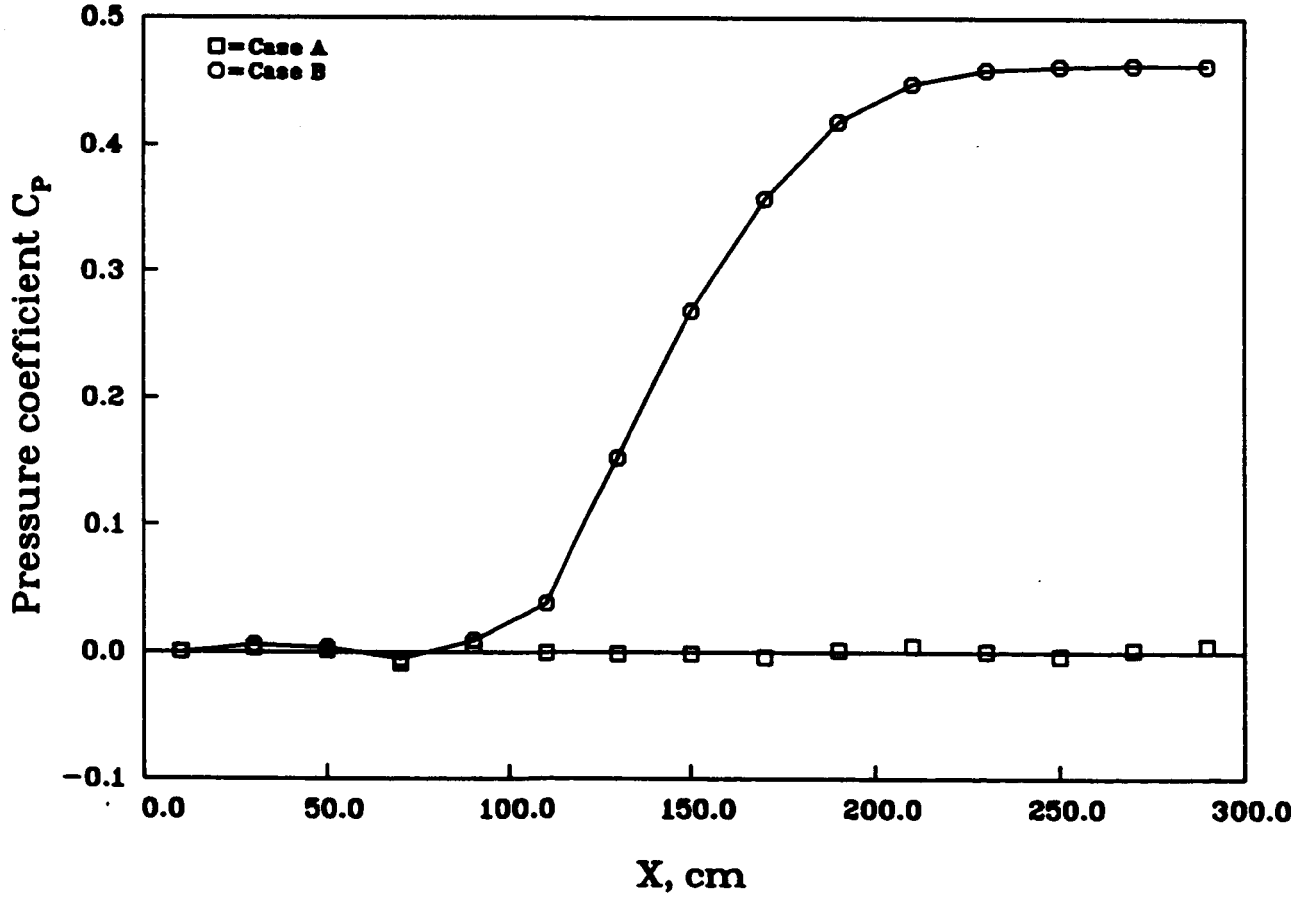

Figure 3. - Cases A and B: measured wall static pressure distributions.

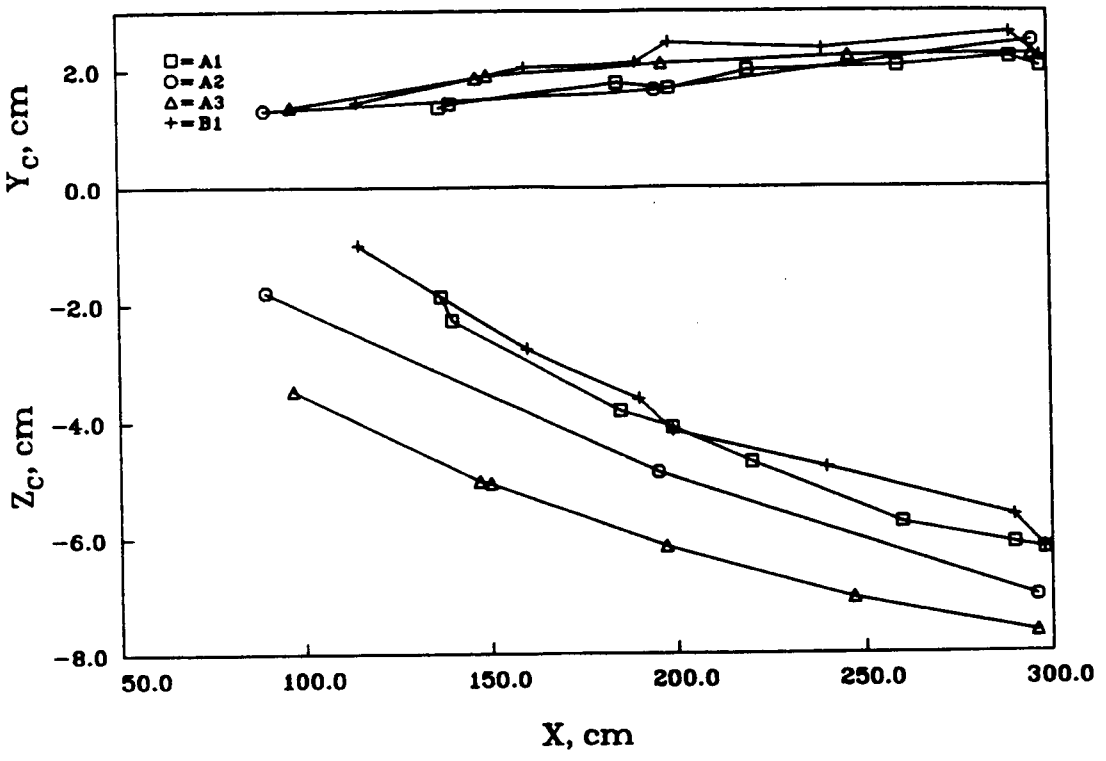

Figure 4. - Vortex core position vs. streamwise location.

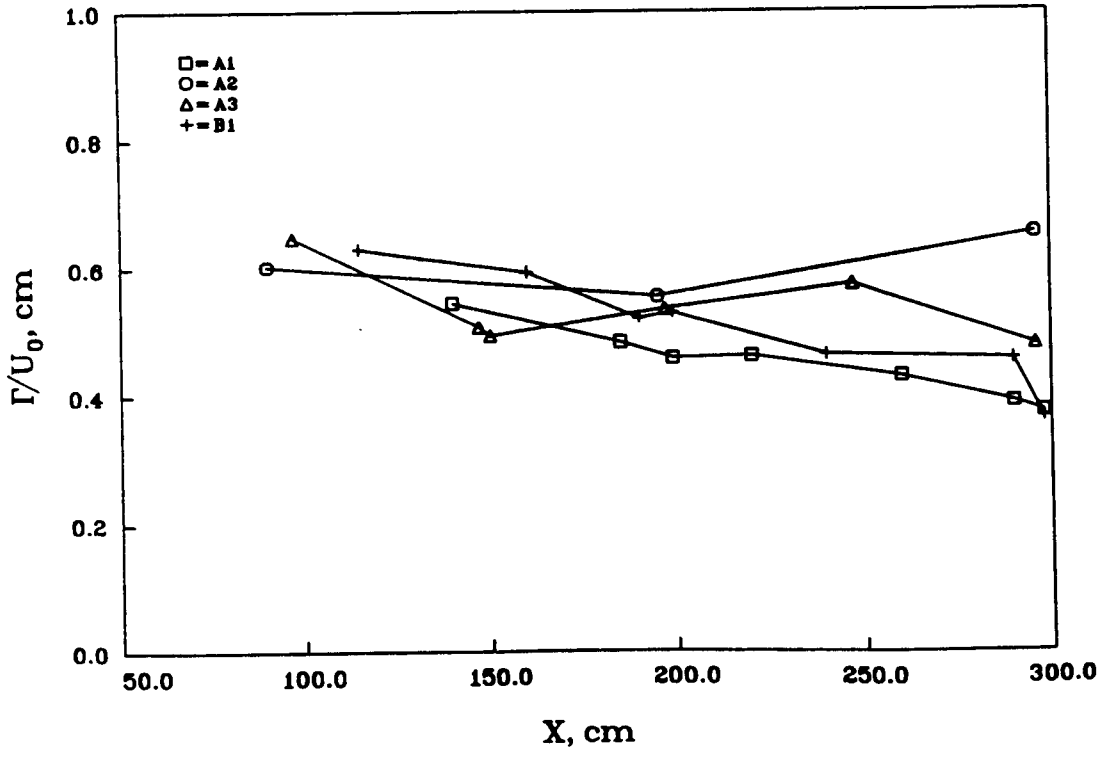

Figure 5. - Vortex circulation vs. streamwise location.

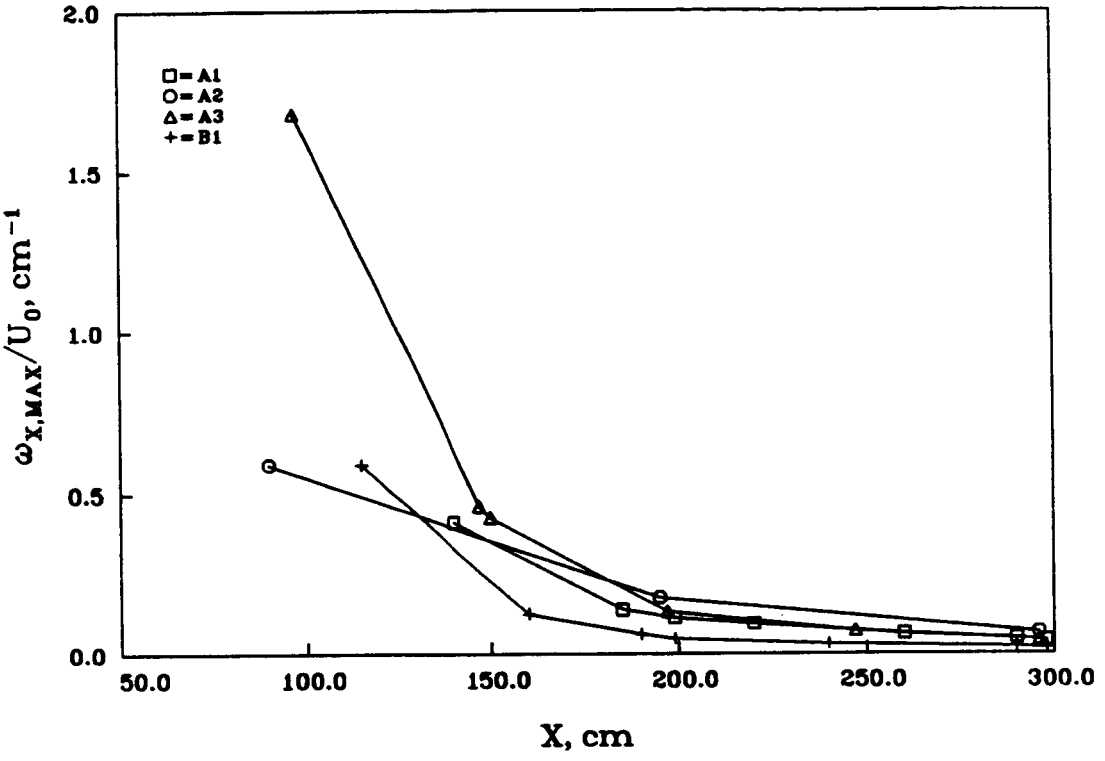

Figure 6. - Vortex core peak vorticity vs. streamwise location.

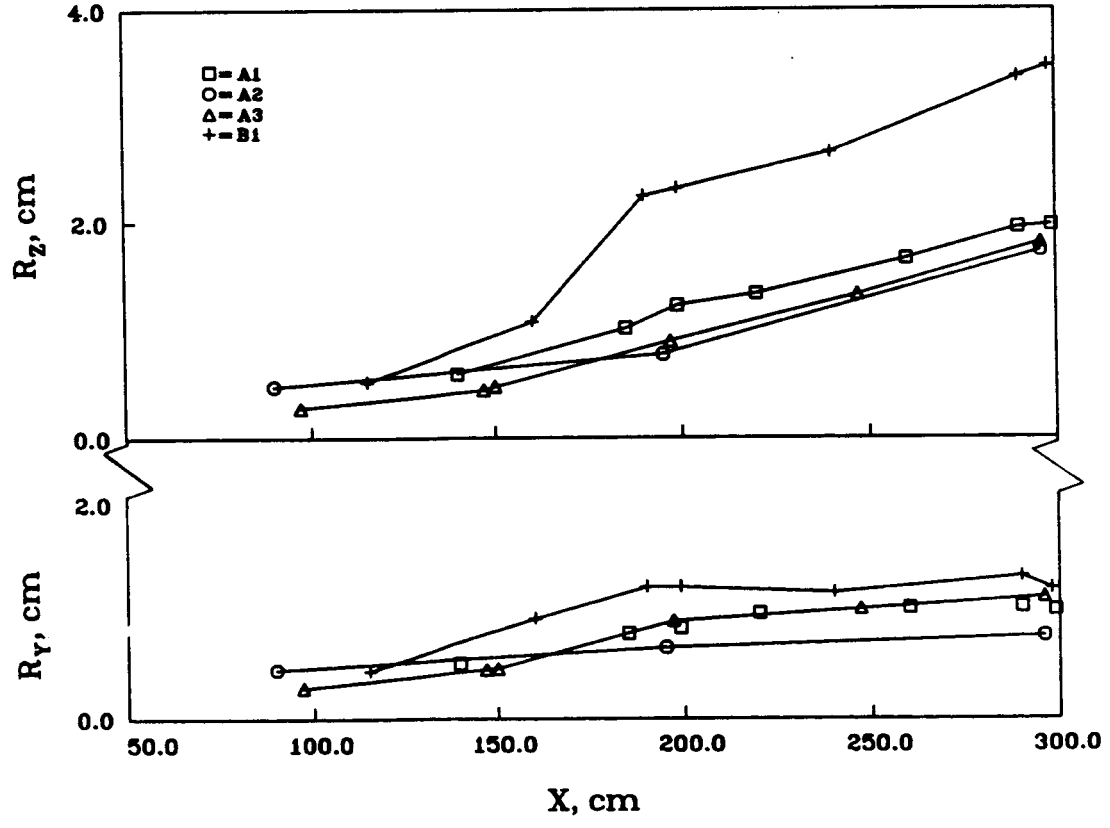

Figure 7. - Vortex core dimensions vs. streamwise location.

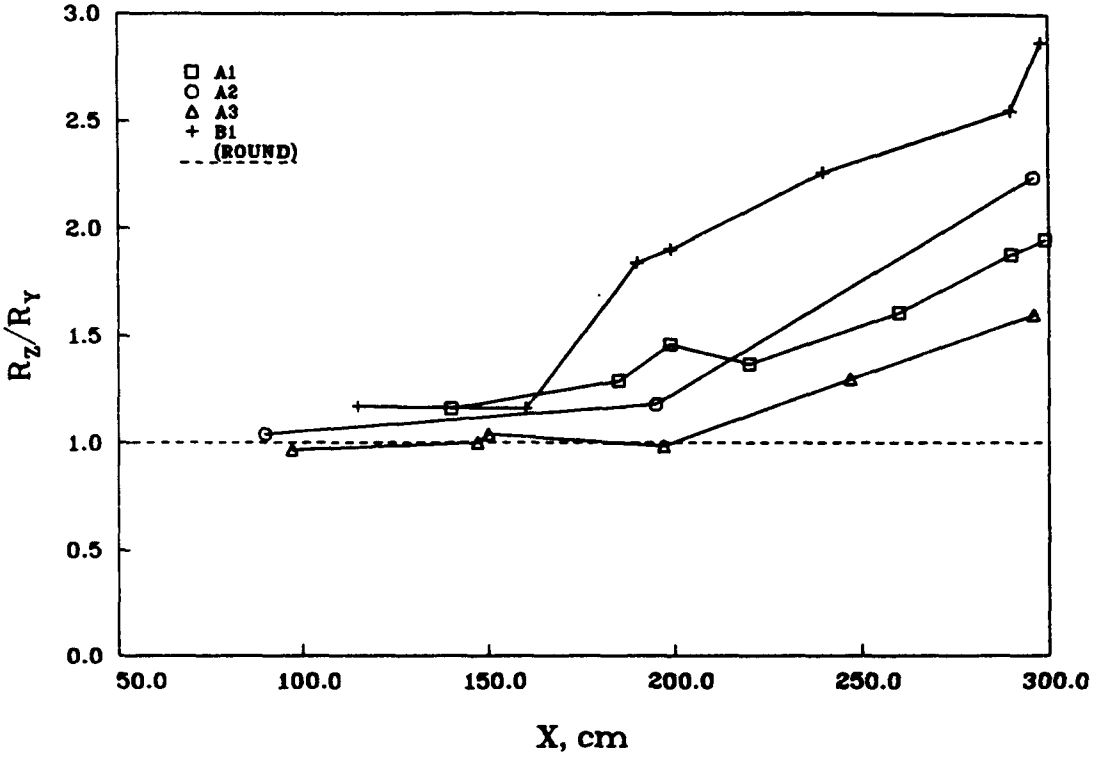

Figure 8. - Vortex core ellipticity vs. streamwise location.

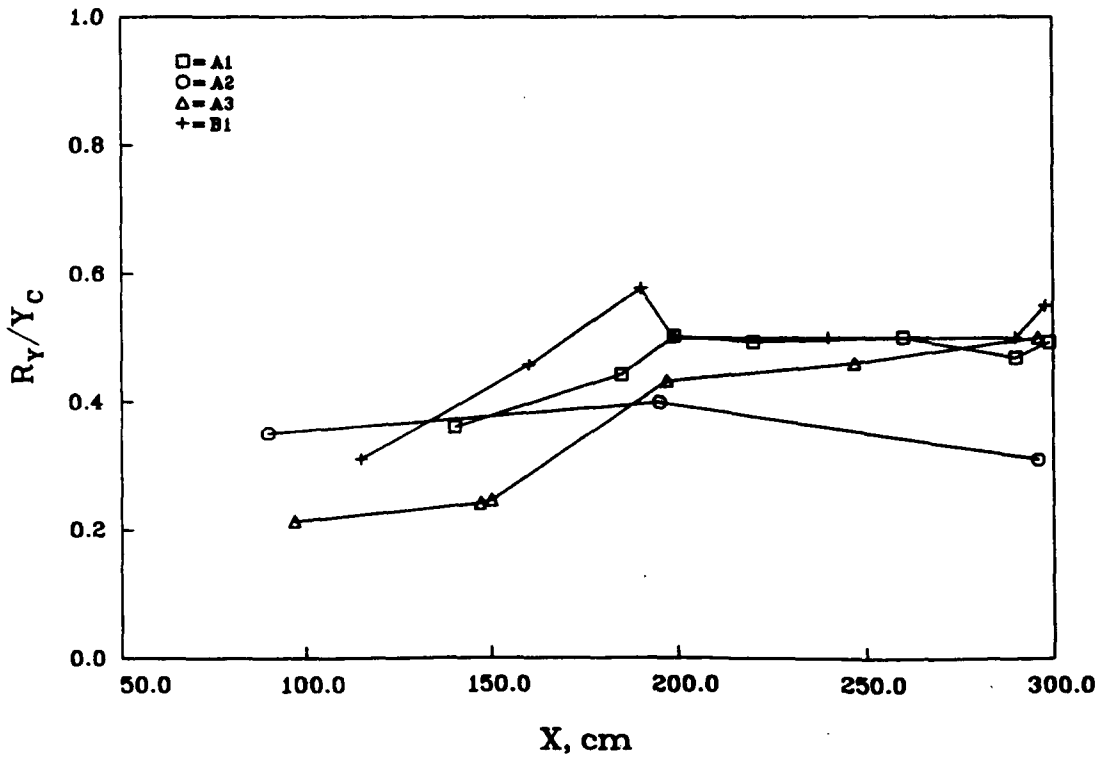

Figure 9. - Nondimensional vortex core vertical extent vs. streamwise location.

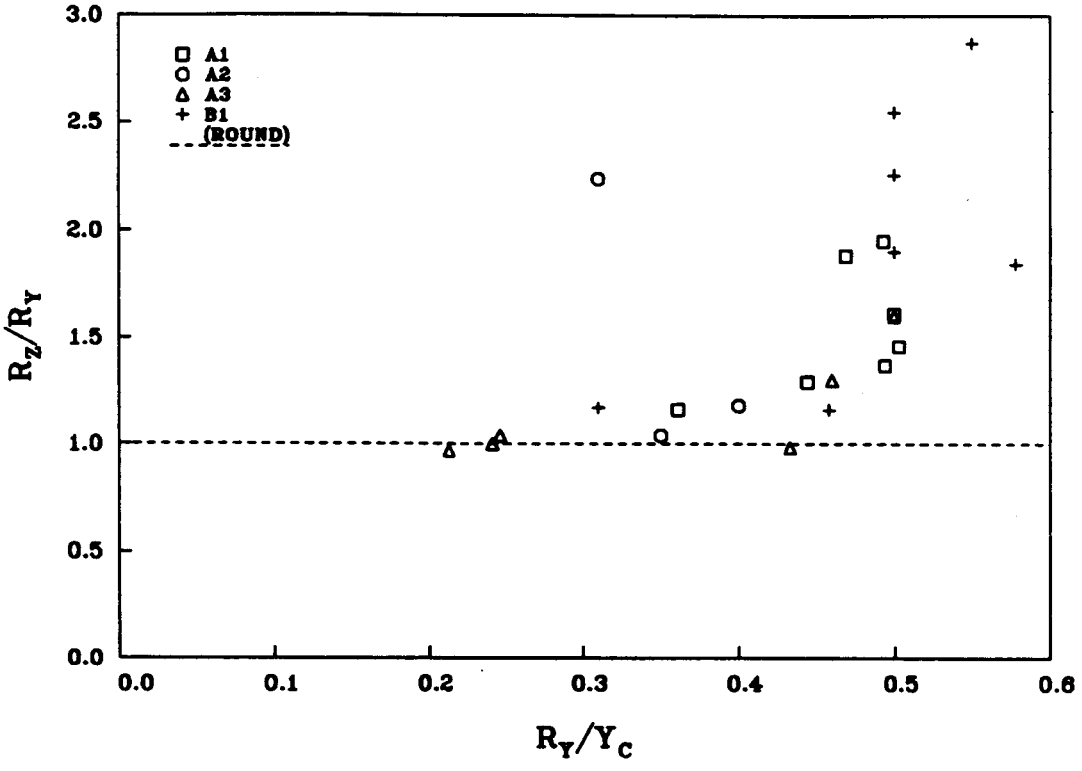

Figure 10. - Vortex core ellipticity vs. nondimensional vortex core vertical extent.

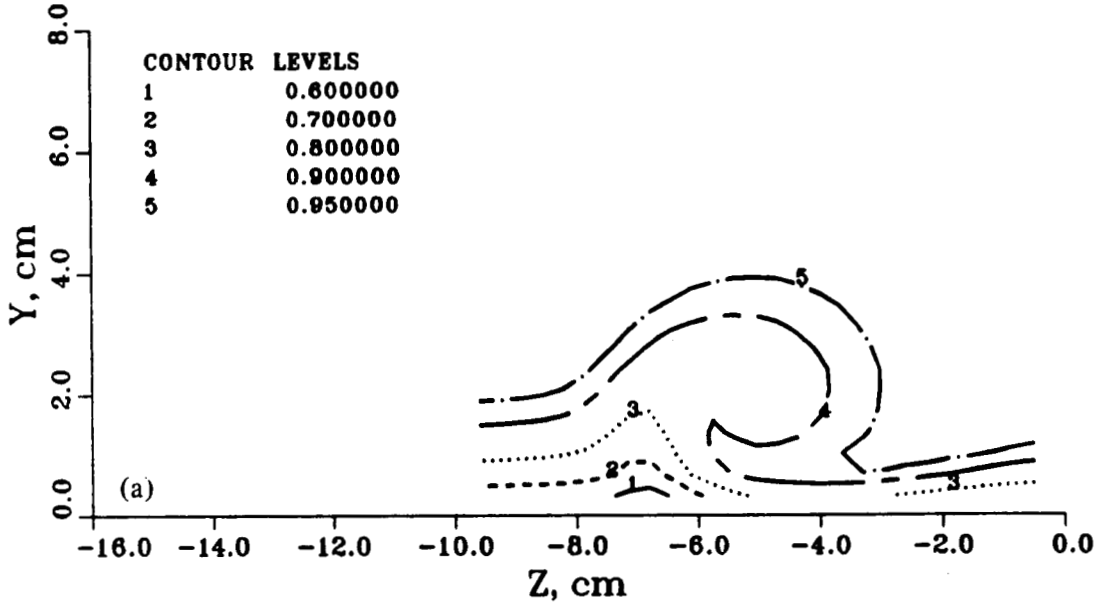

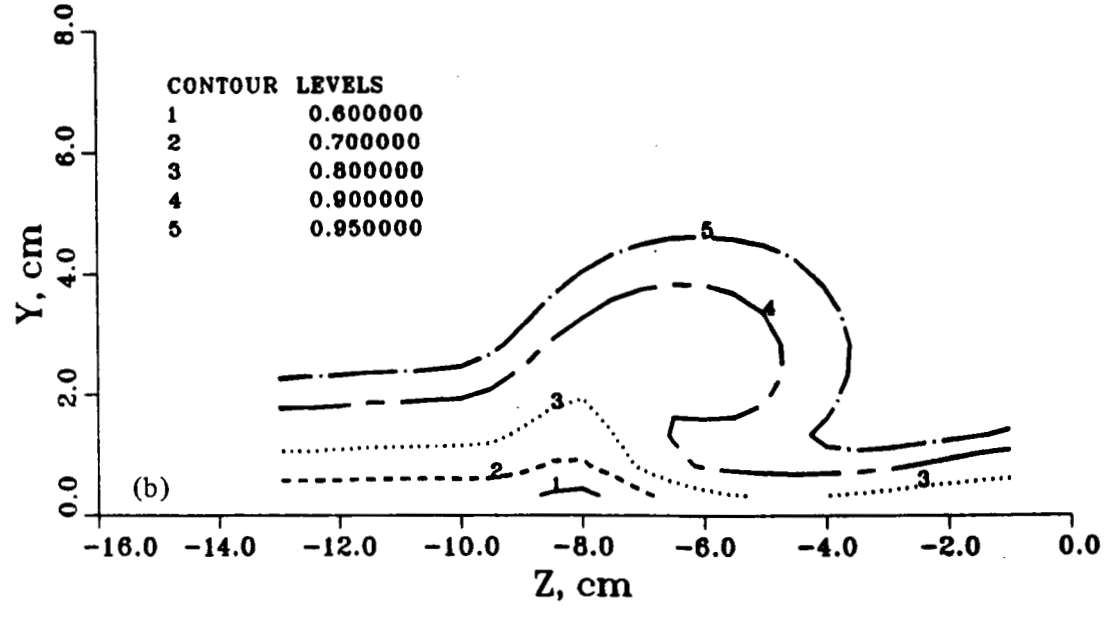

Figure 11. - Streamwise velocity contours, U/U_0, Case A3, at four streamwise positions. (a) $X = 150$ cm. (b) $X = 195$ cm.

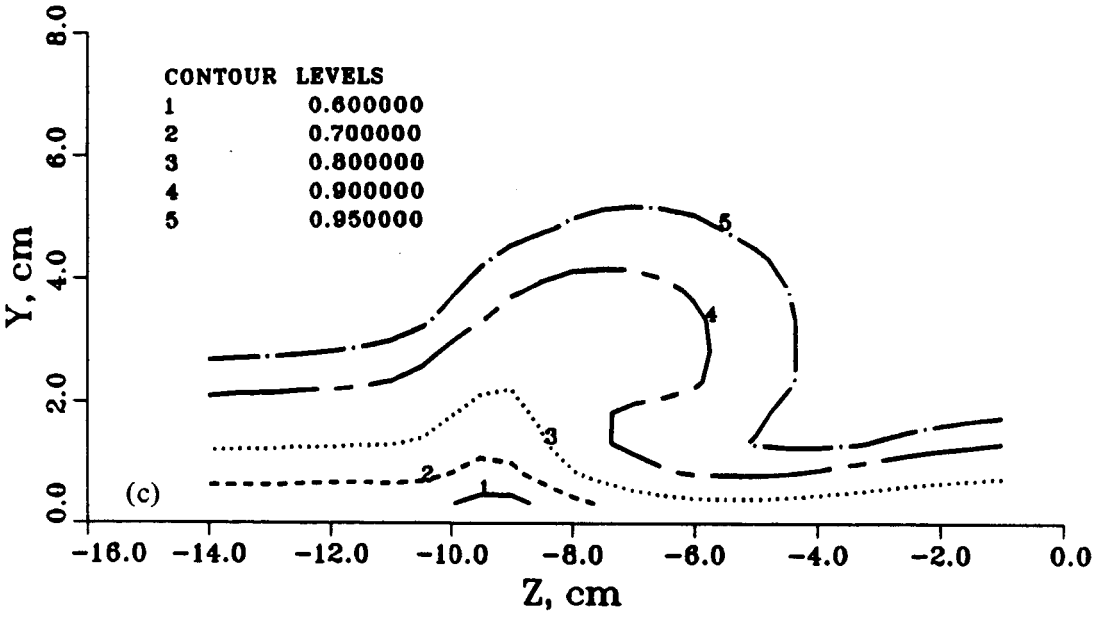

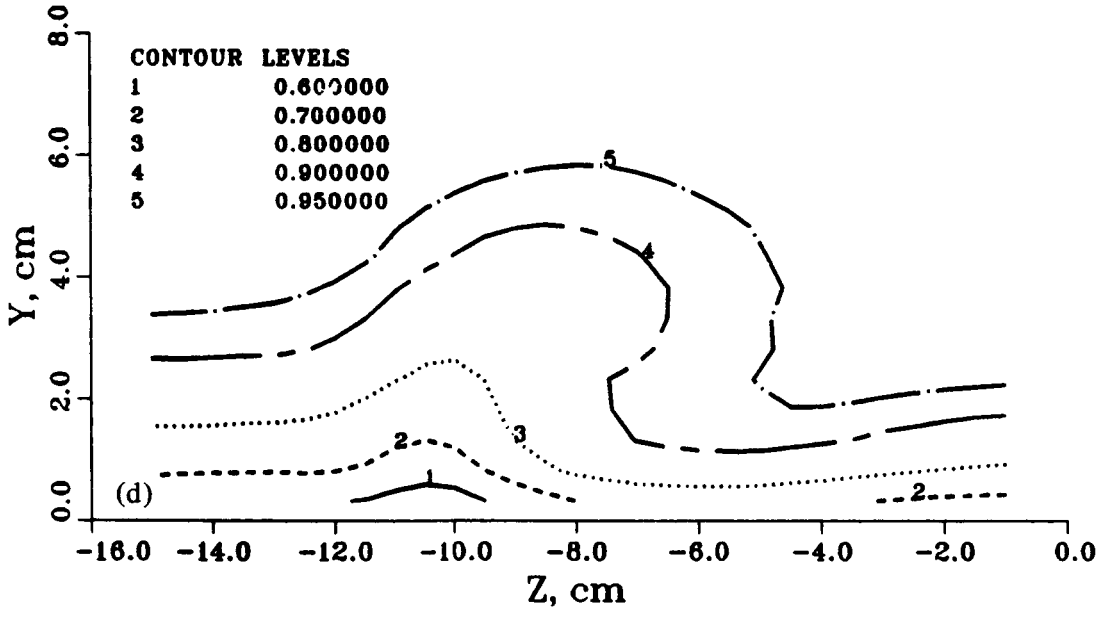

Figure 11. - Concluded. (c) X = 240 cm. (d) X = 295 cm.

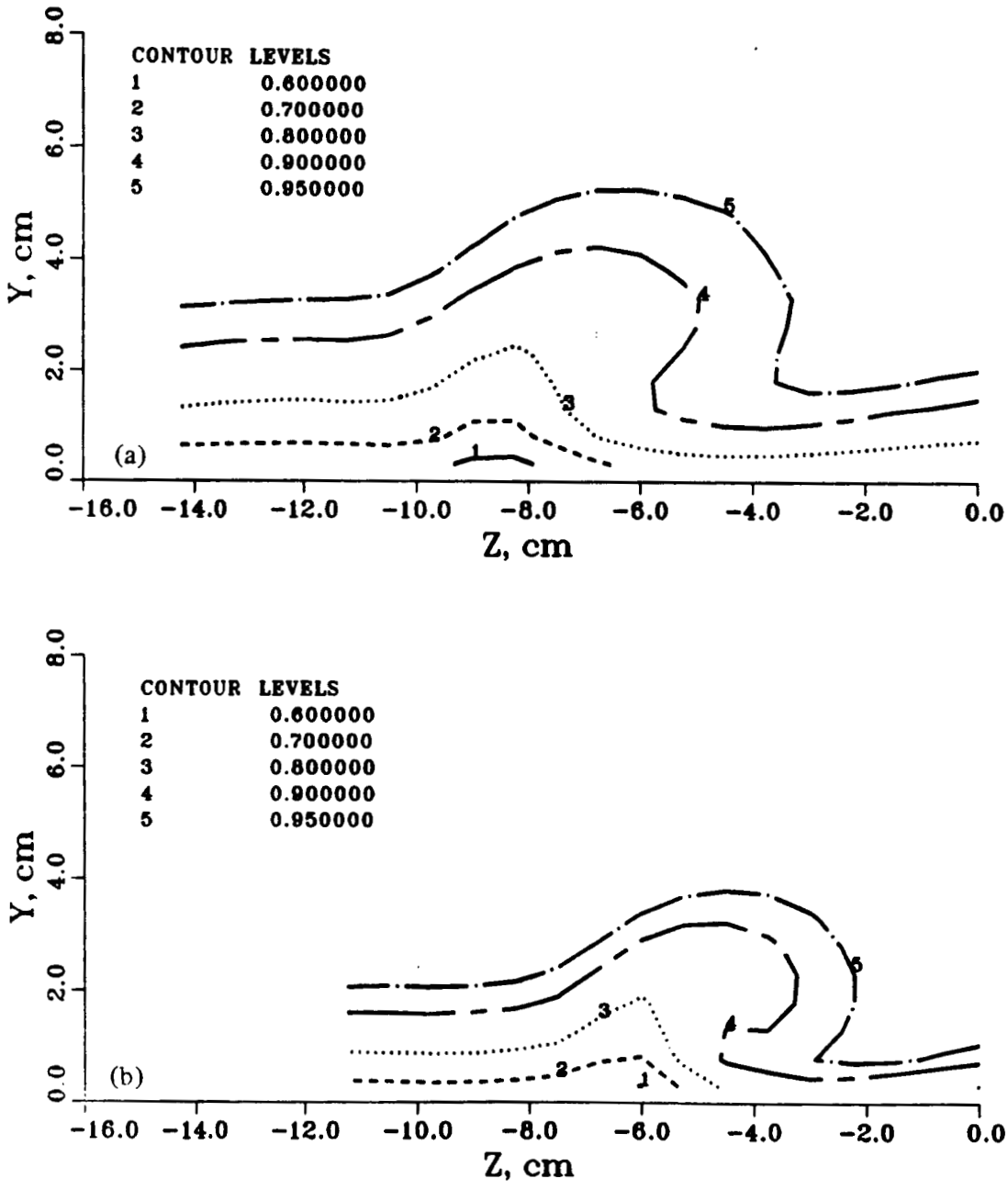

Figure 12. - Streamwise velocity contours, U/U_0, Case A1, at two streamwise positions. (a) $X = 199$ cm. (b) $X = 298$ cm.

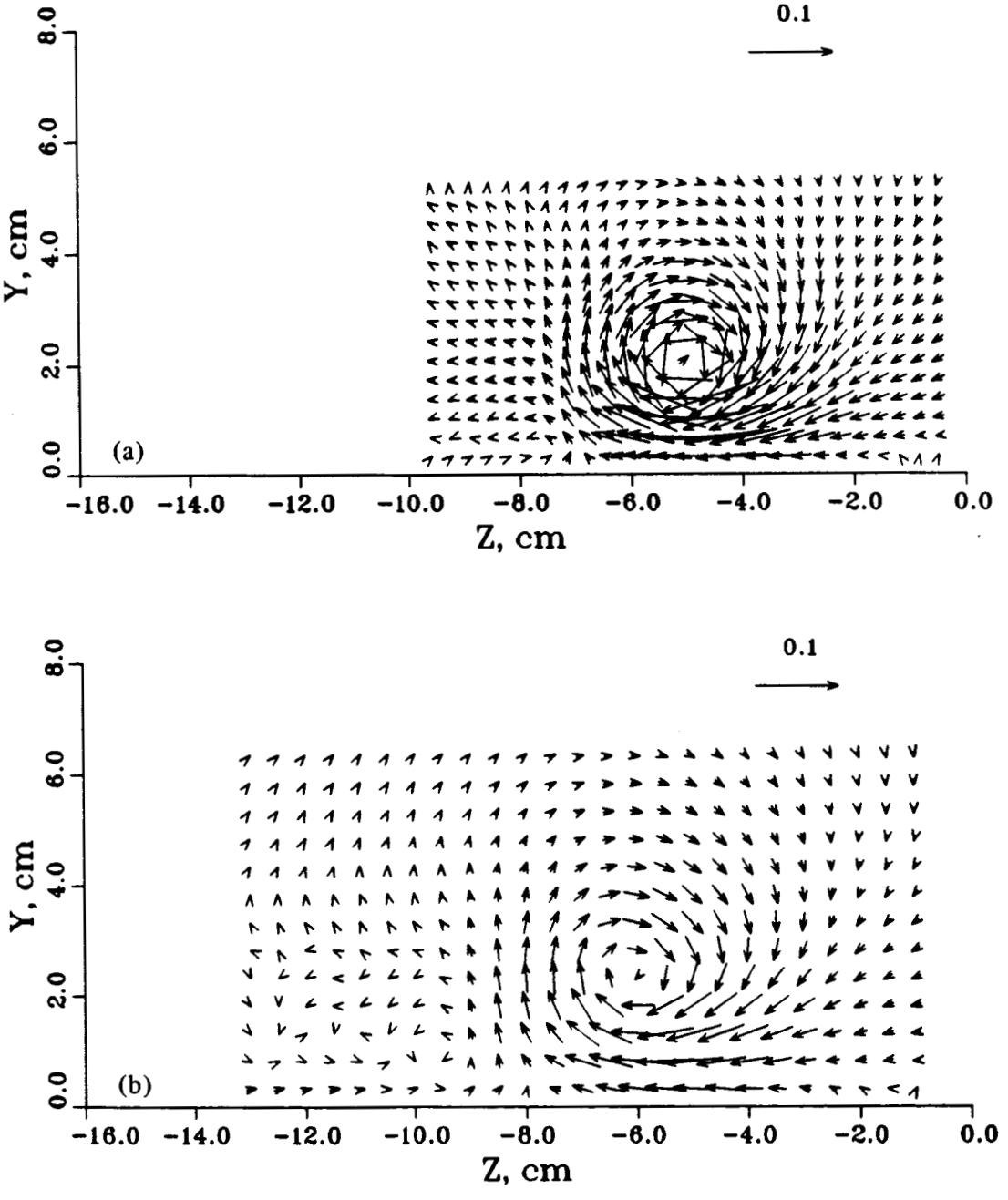

Figure 13. - Cross-flow plane velocity vectors V/U_0, W/U_0, Case A3, at four streamwise positions. (a) X = 150 cm. (b) X = 195 cm.

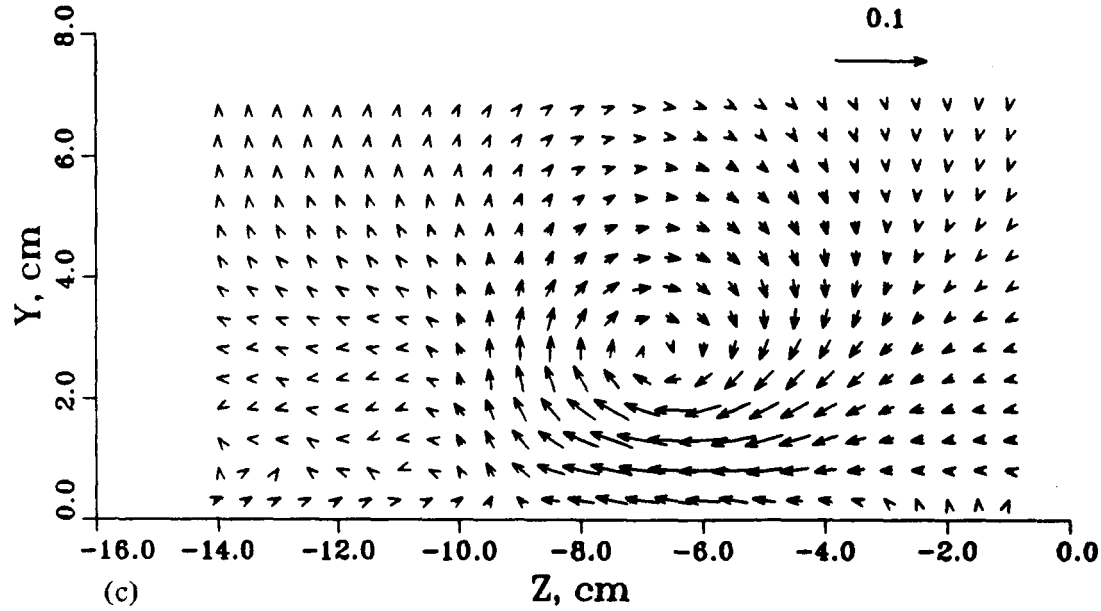

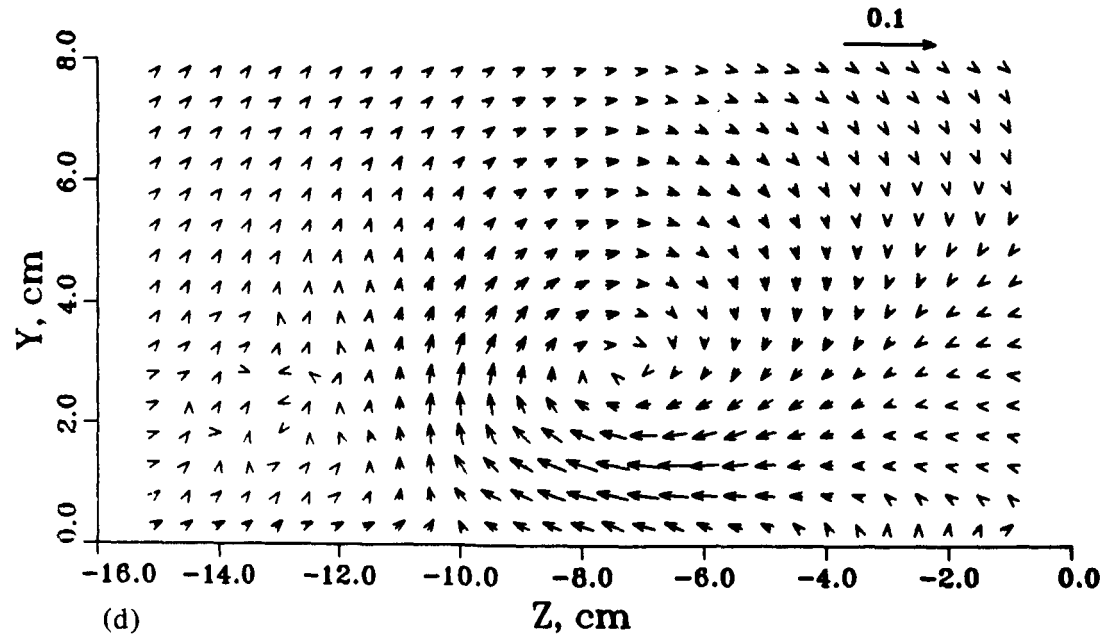

Figure 13. - Concluded. (c) X = 240 cm. (d) X = 295 cm.

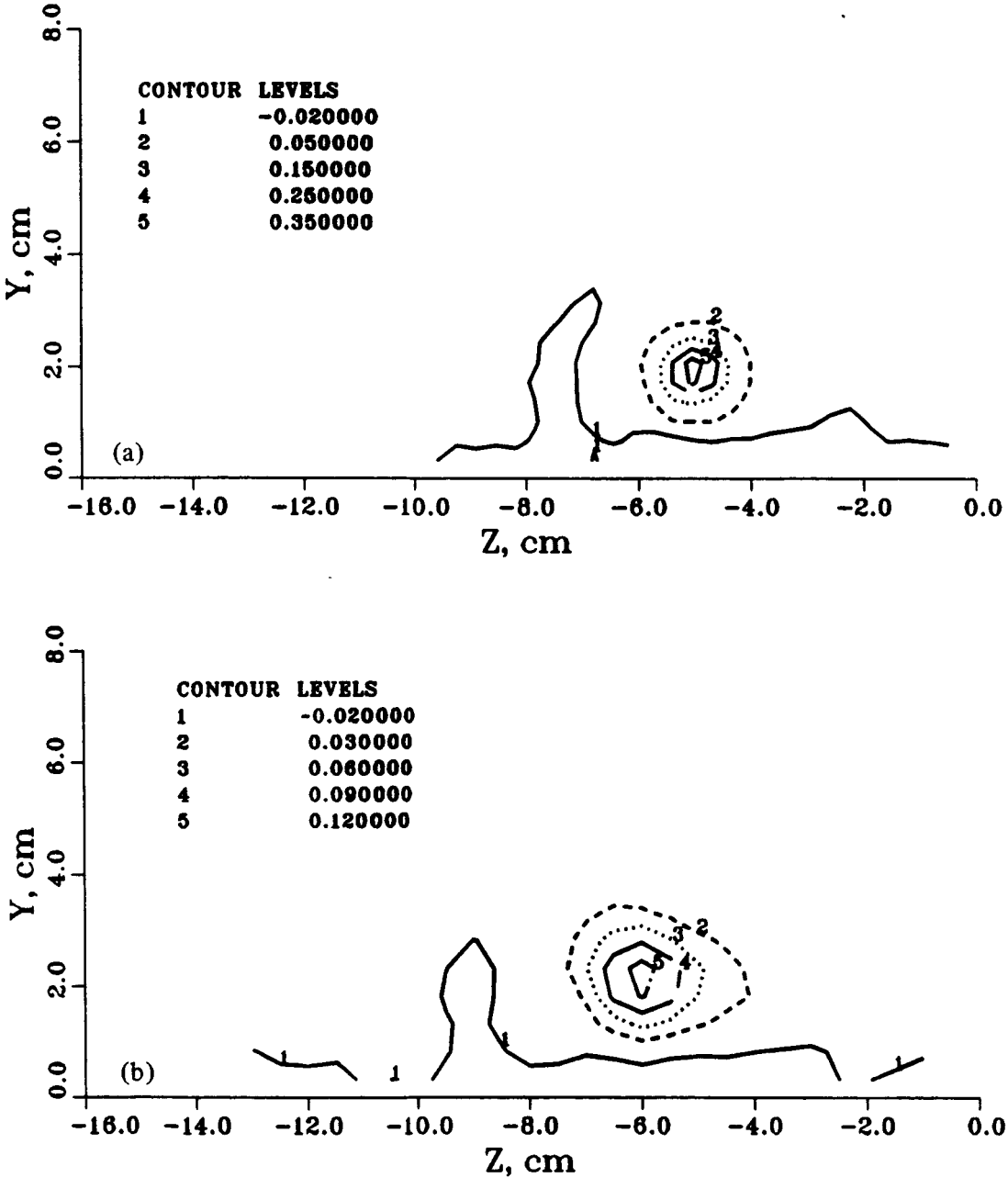

Figure 14. - Streamwise vorticity contours, ω_X/U_0, cm, Case A3, at four streamwise positions. (a) $X = 150$ cm. (b) $X = 195$ cm.

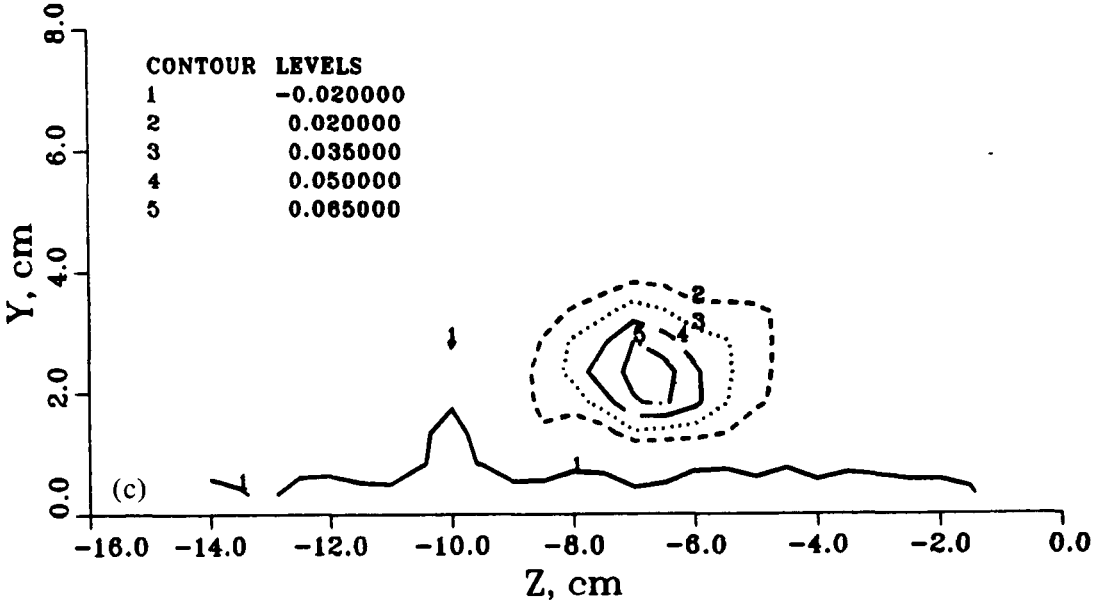

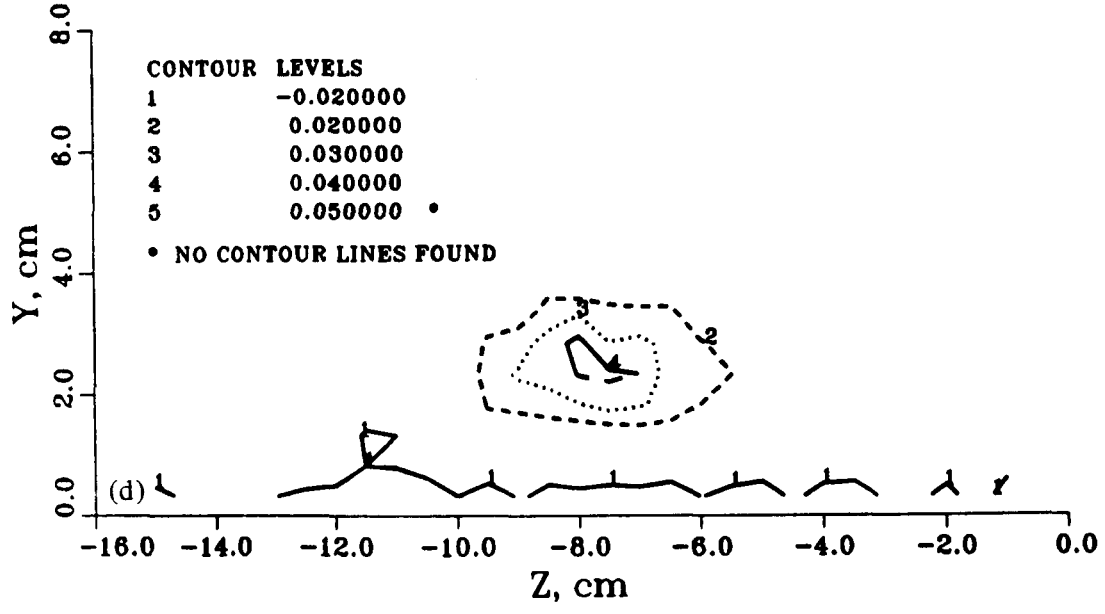

Figure 14.- Concluded. (c) X = 240 cm. (d) X = 295 cm.

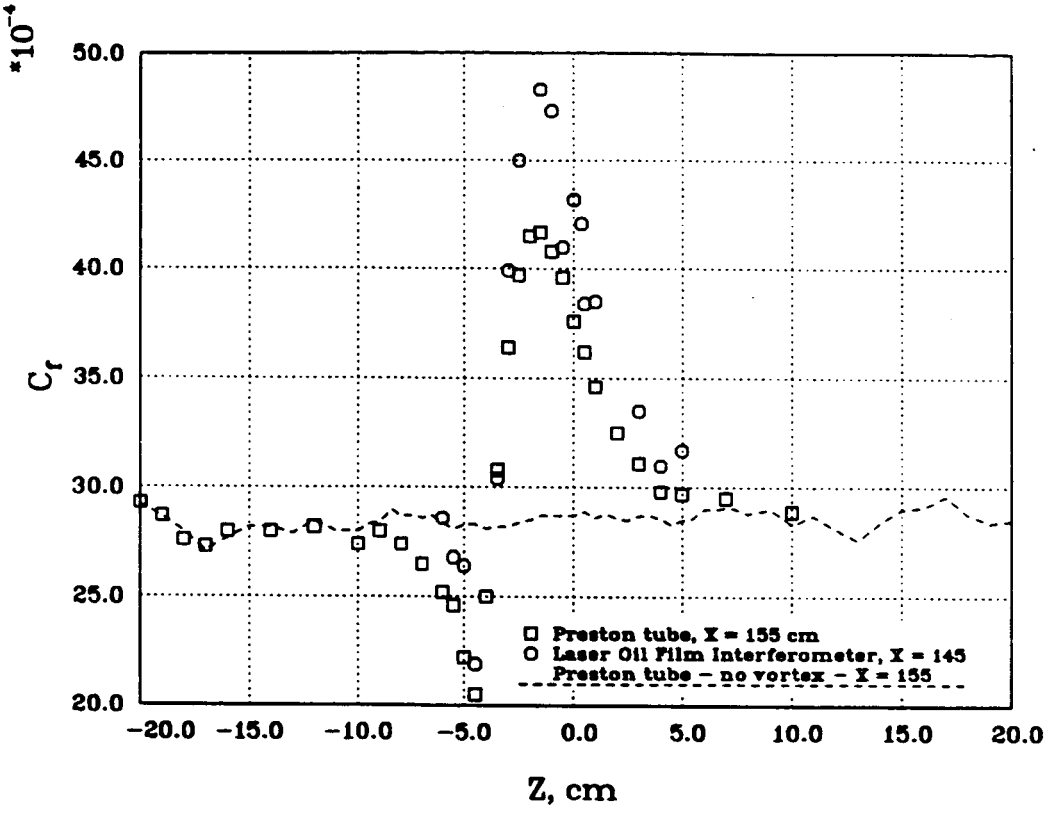

Figure 15. - Oil film and Preston tube skin friction data, Case A1, near $X = 150$ cm.

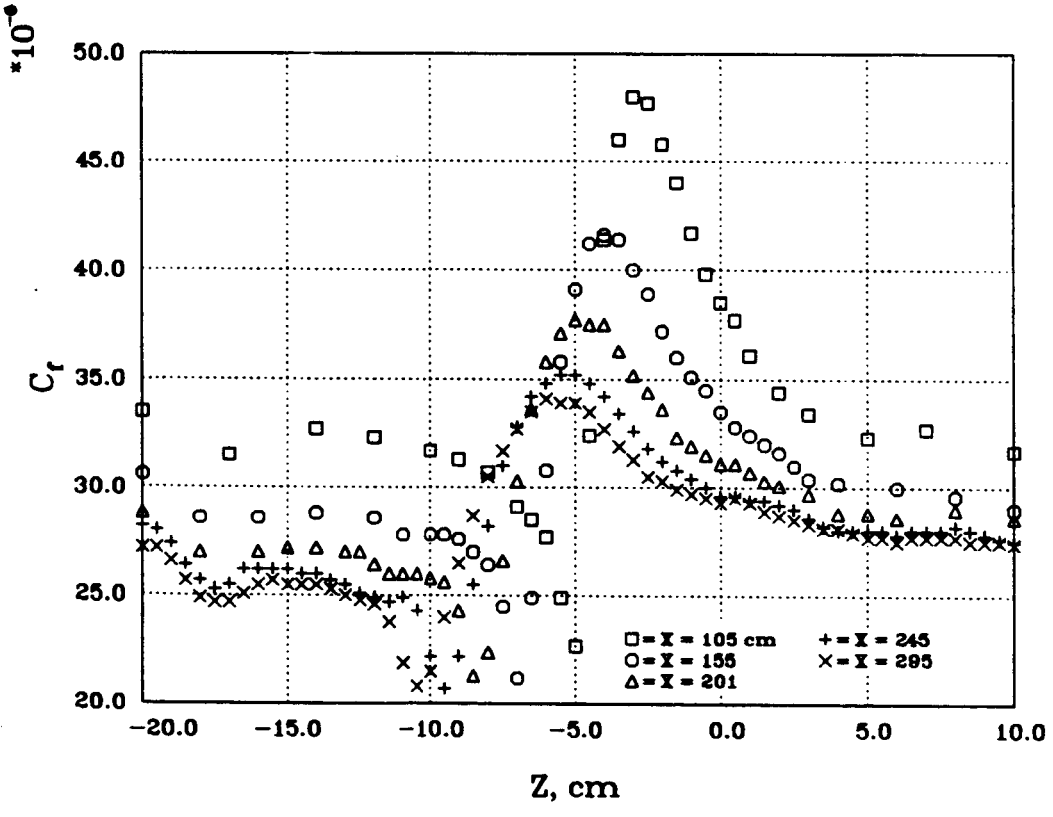

Figure 16. - Preston tube skin friction data, Case A3.

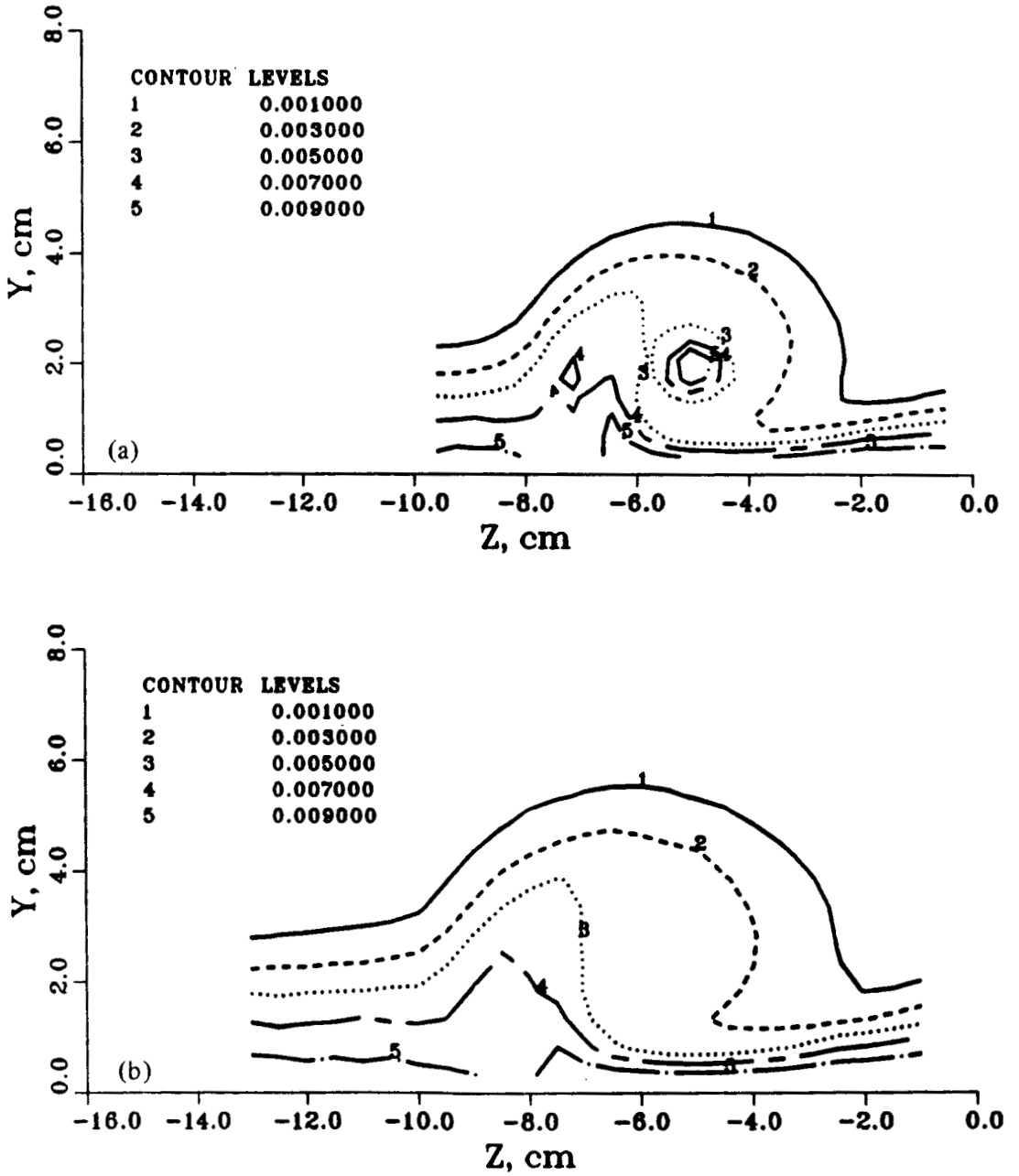

Figure 17. - Turbulence kinetic energy contours, q^2/U_0^2, Case A3, at four streamwise positions. (a) X = 150 cm. (b) X = 195 cm.

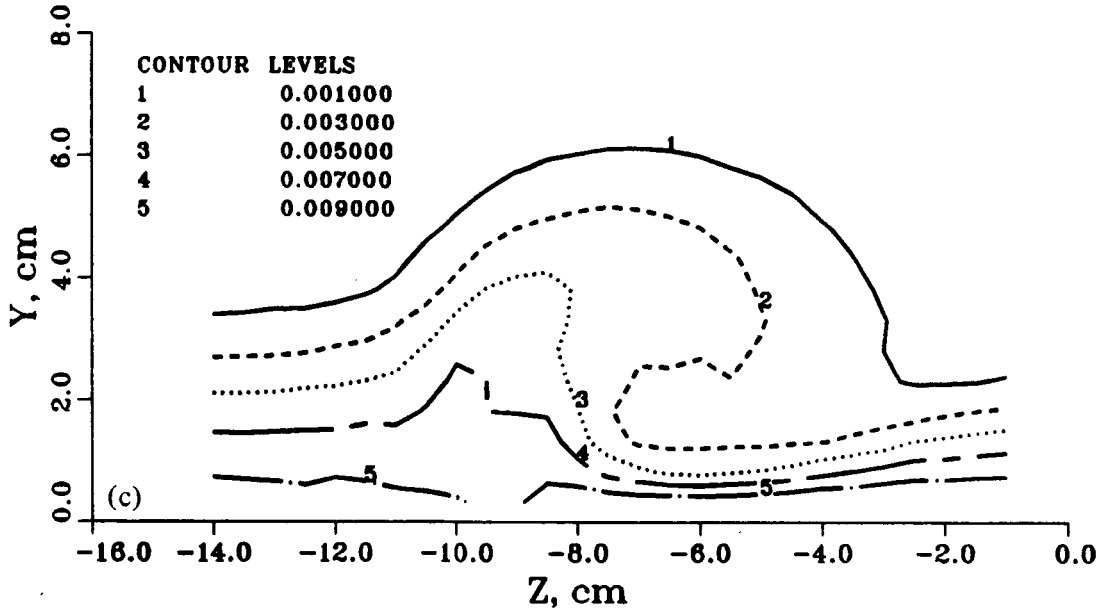

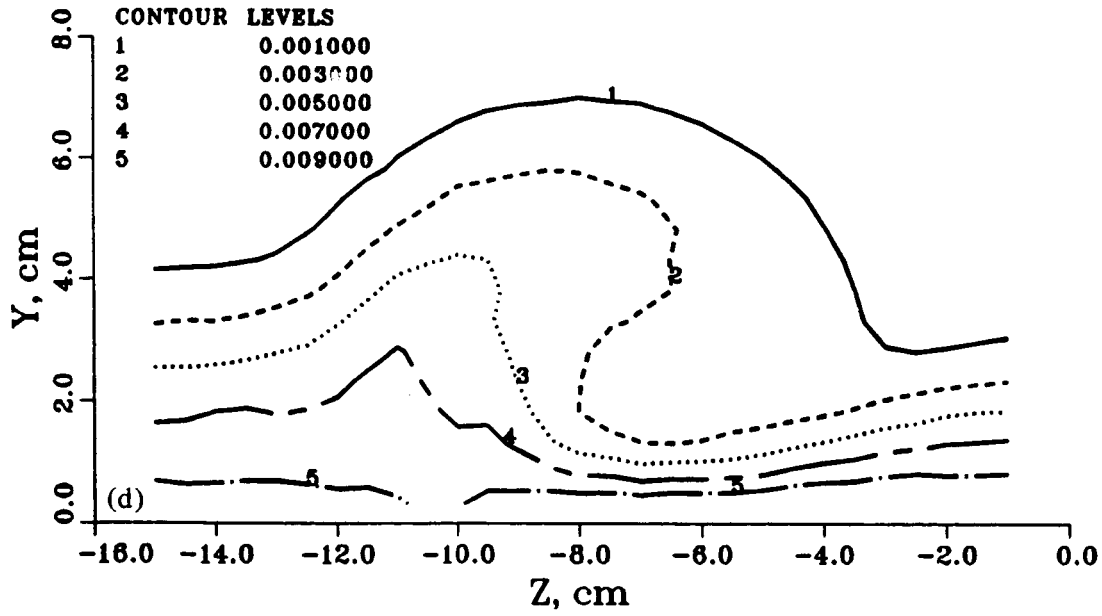

Figure 17. - Concluded. (c) X = 240 cm. (d) X = 295 cm.

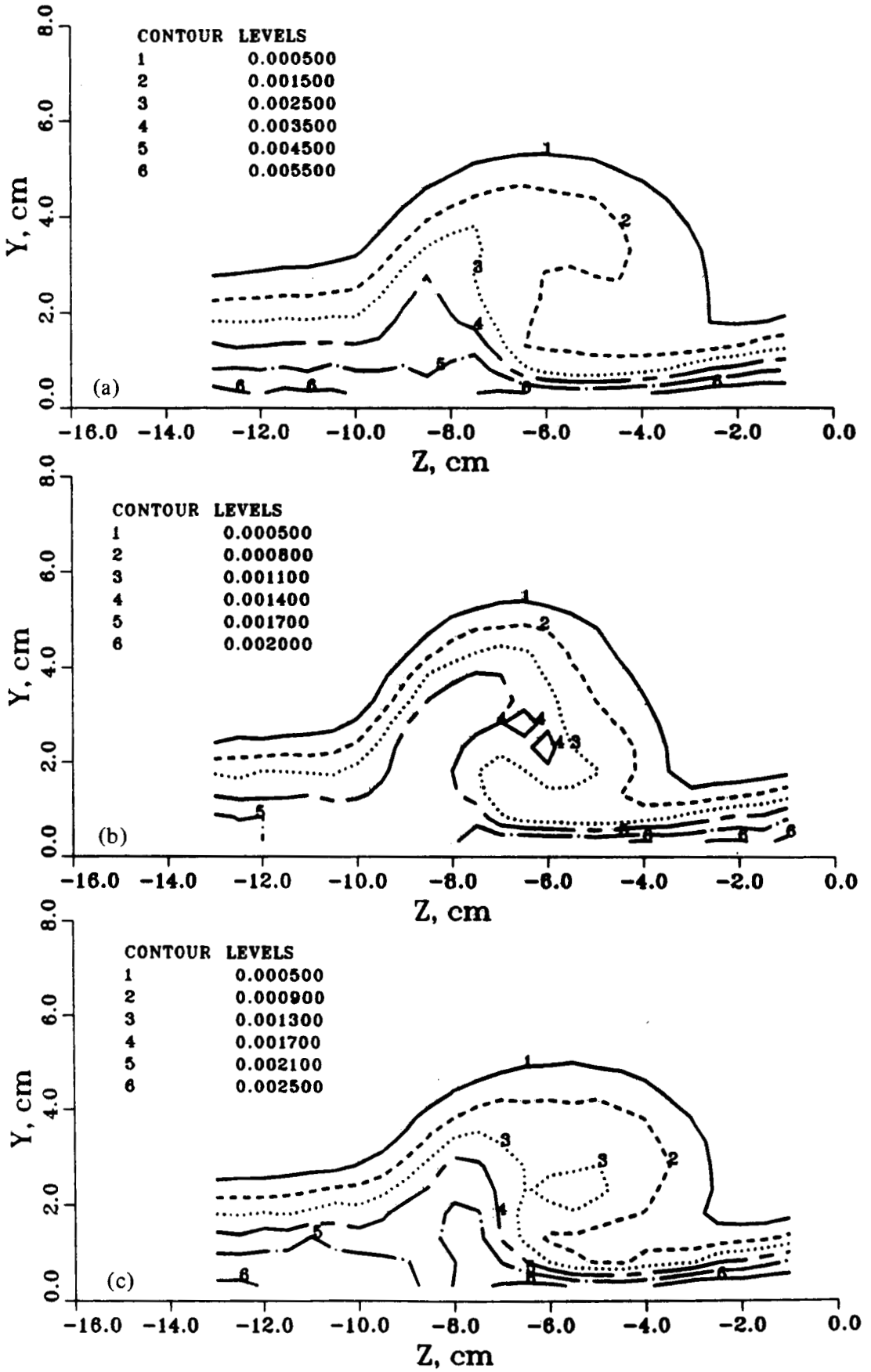

Figure 18. - Turbulence normal stress contours, $X = 195$ cm, Case A3. (a) $\overline{u'^2}/U_0^2$. (b) $\overline{v'^2}/U_0^2$. (c) $\overline{w'^2}/U_0^2$.

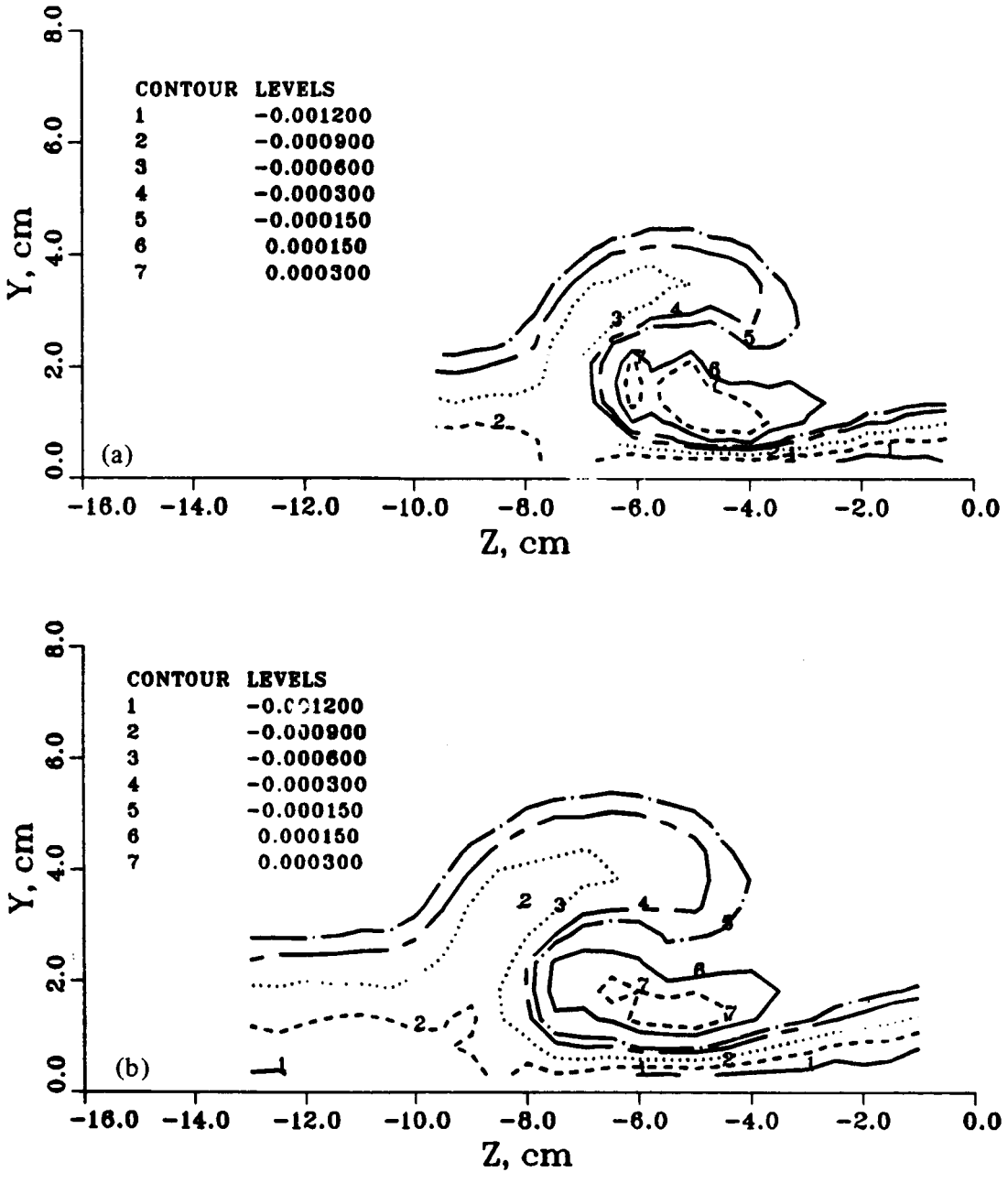

Figure 19. $X - Y$ plane turbulence shear stress ($\overline{u'v'}/U_0^2$) contours, Case A3, at four streamwise positions. (a) $X = 150$ cm. (b) $X = 195$ cm.

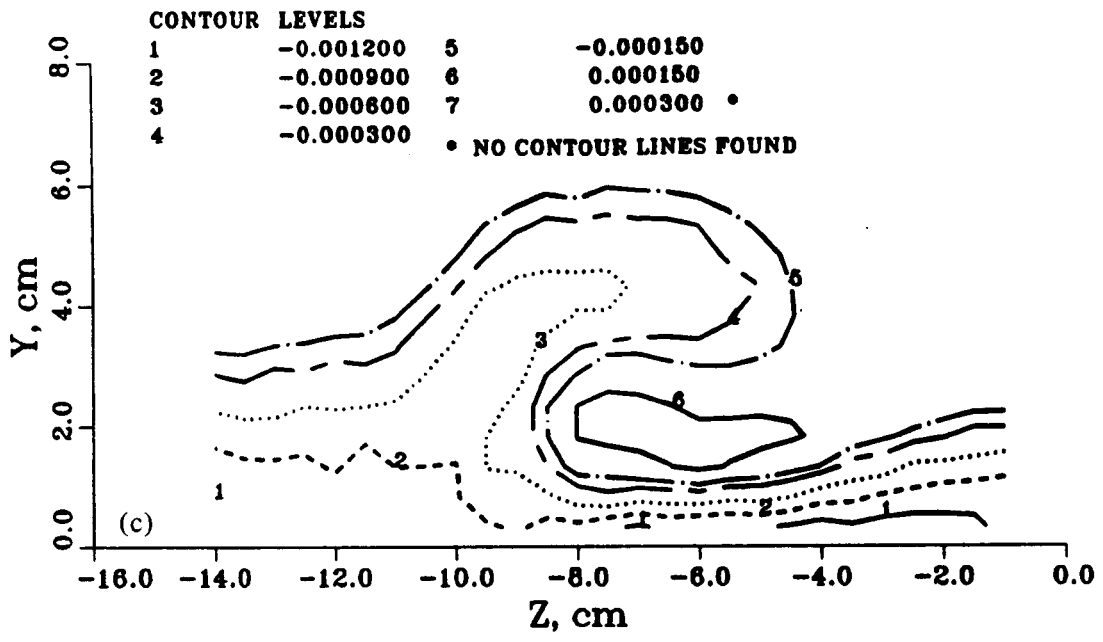

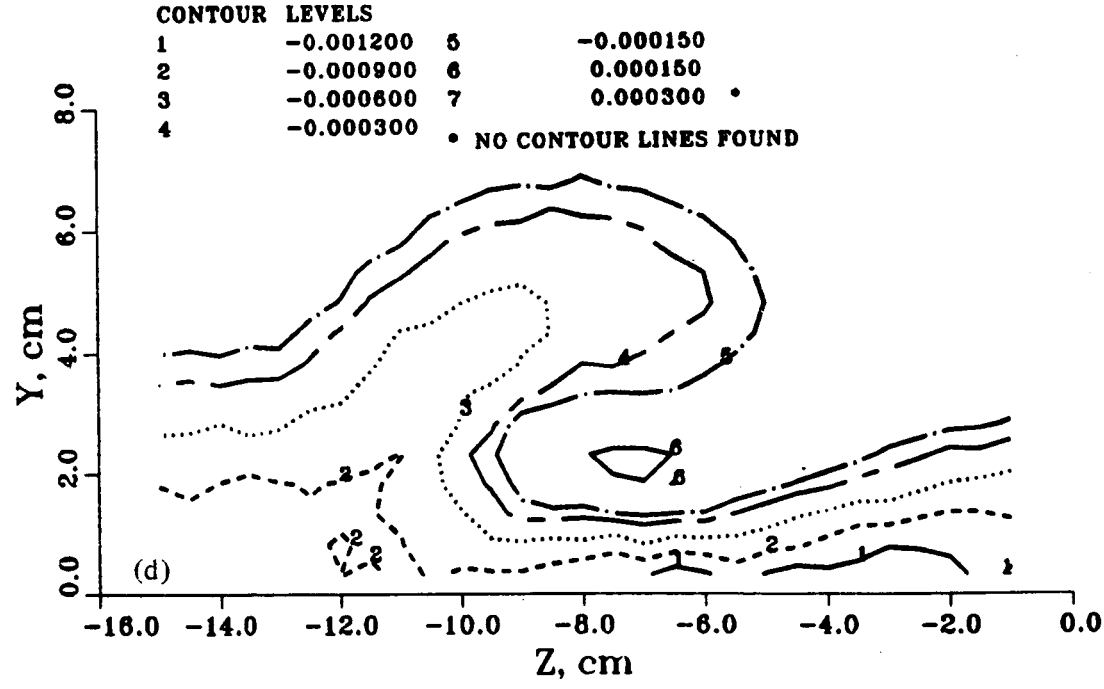

Figure 19. - Concluded. (c) X = 240 cm. (d) X = 295 cm.

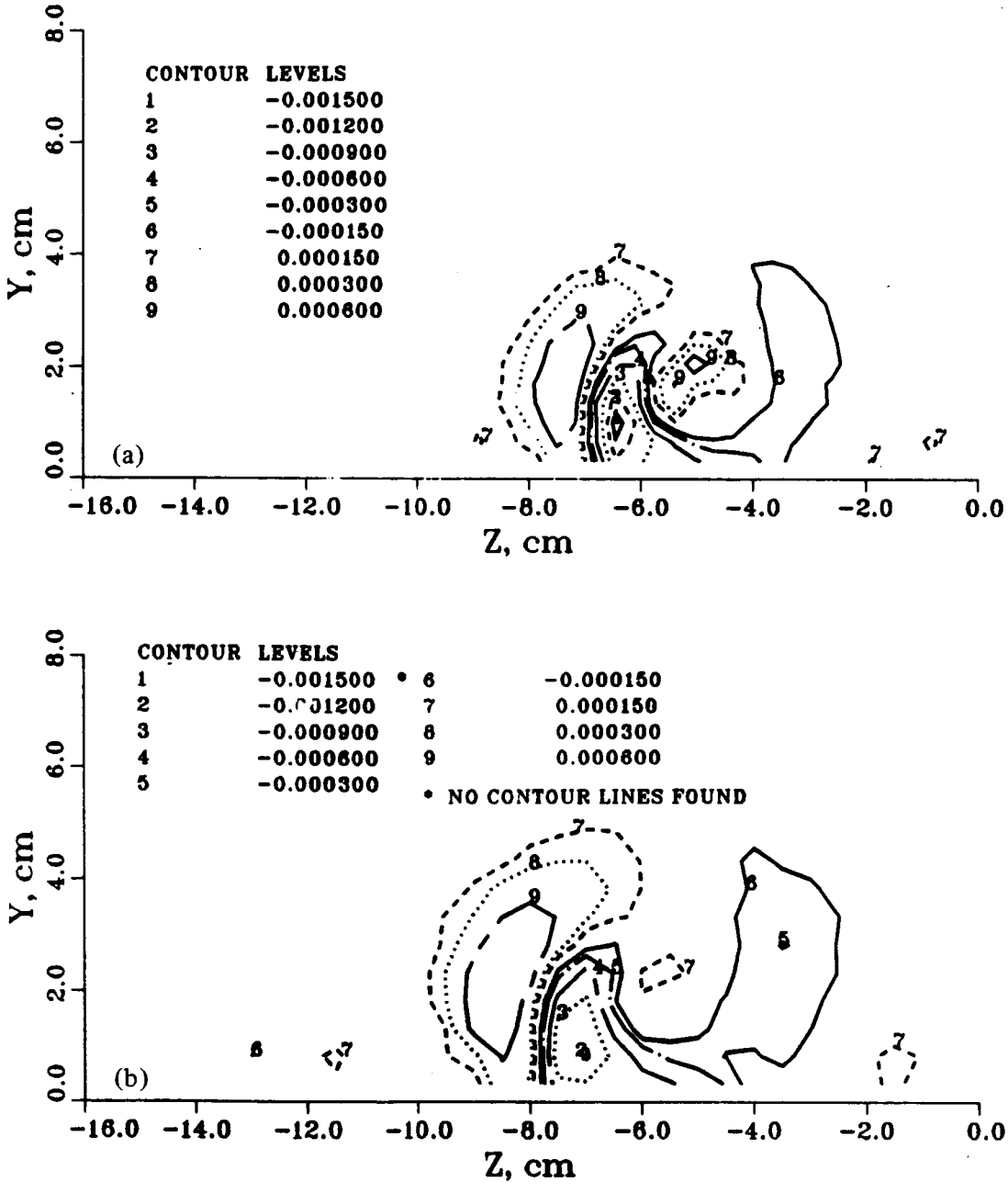

Figure 20. - $X - Z$ plane turbulence shear stress ($\overline{u'w'}/U_0^2$) contours, Case A3, at four streamwise positions. (a) $X = 150$ cm. (b) $X = 195$ cm.

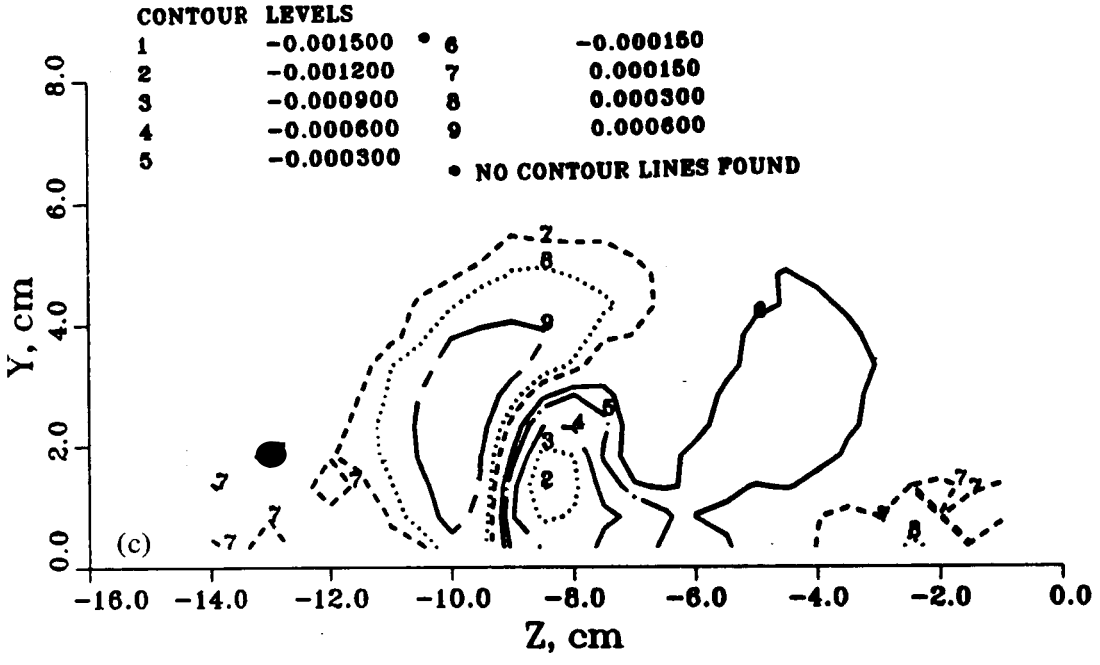

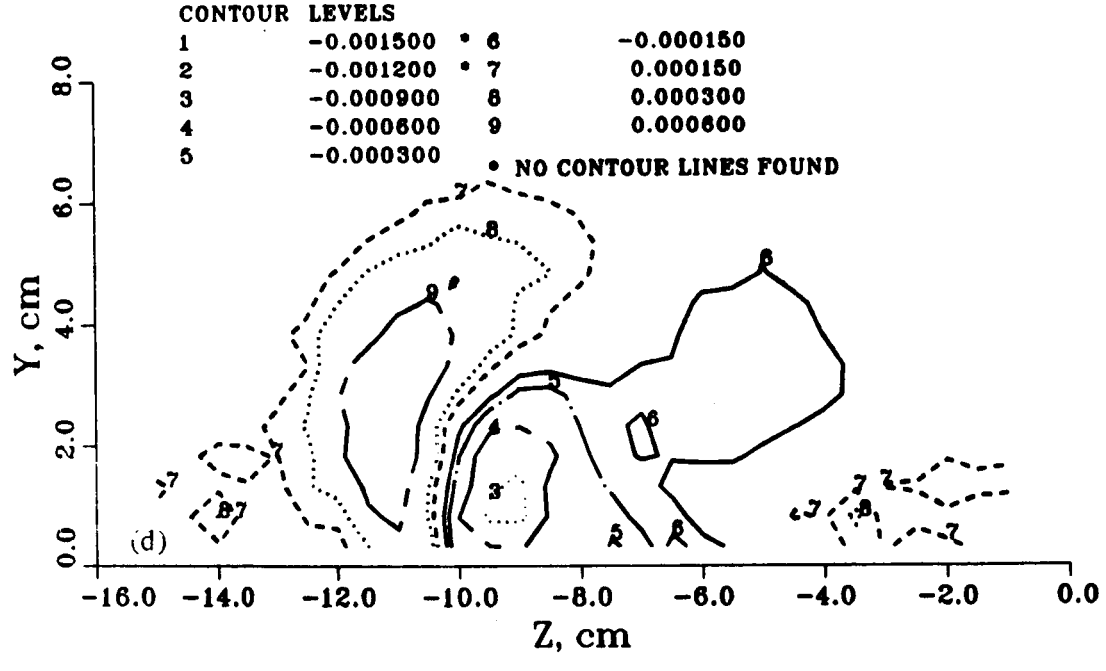

Figure 20. - Concluded. (c) X = 240 cm. (d) X = 295 cm.

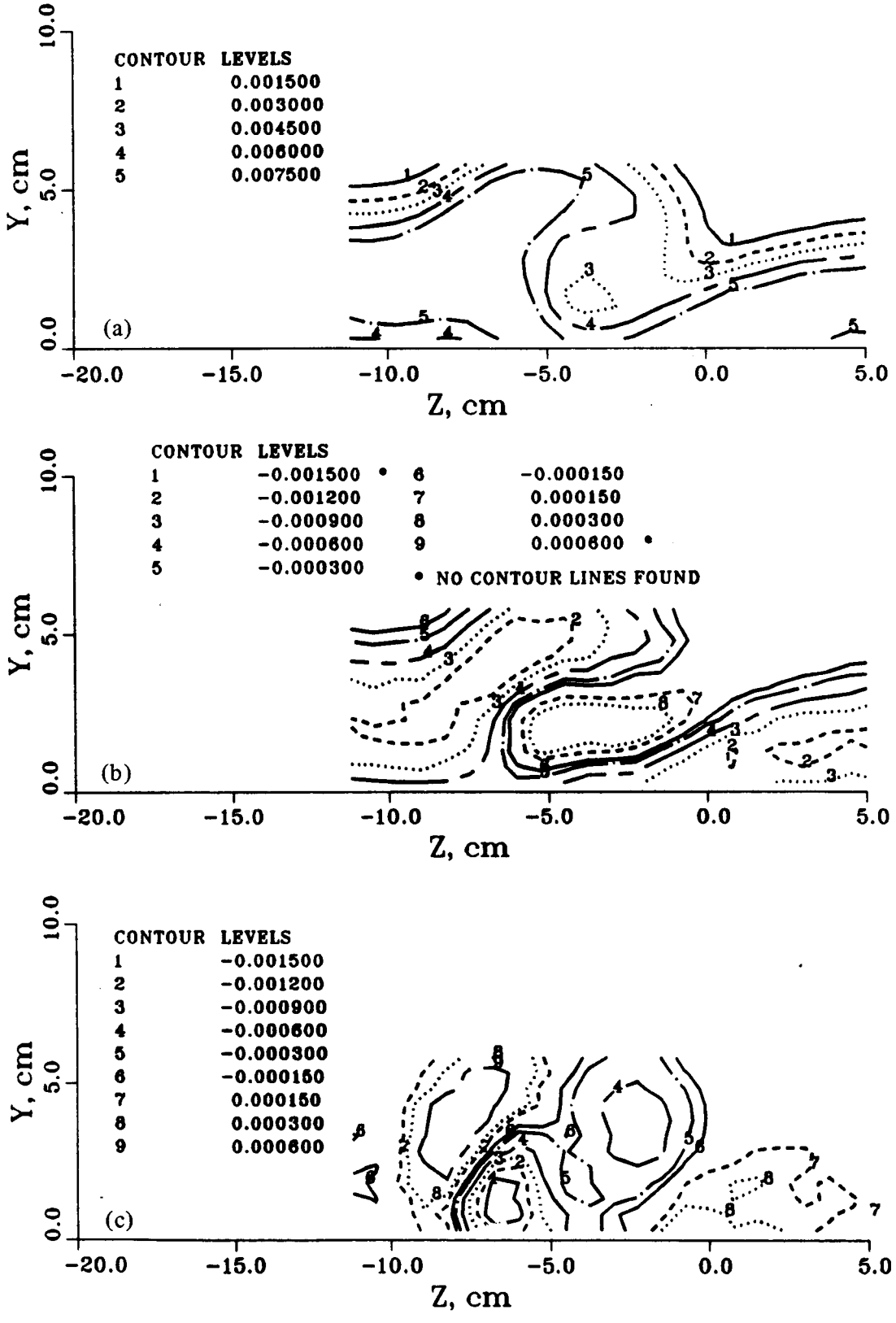

Figure 21. - Sample turbulence data in adverse pressure gradeint, Case B1, X = 199 cm. (a) $\overline{q^2}/U_0^2$. (b) $\overline{u'v'}/U_0^2$. (c) $\overline{u'w'}/U_0^2$.

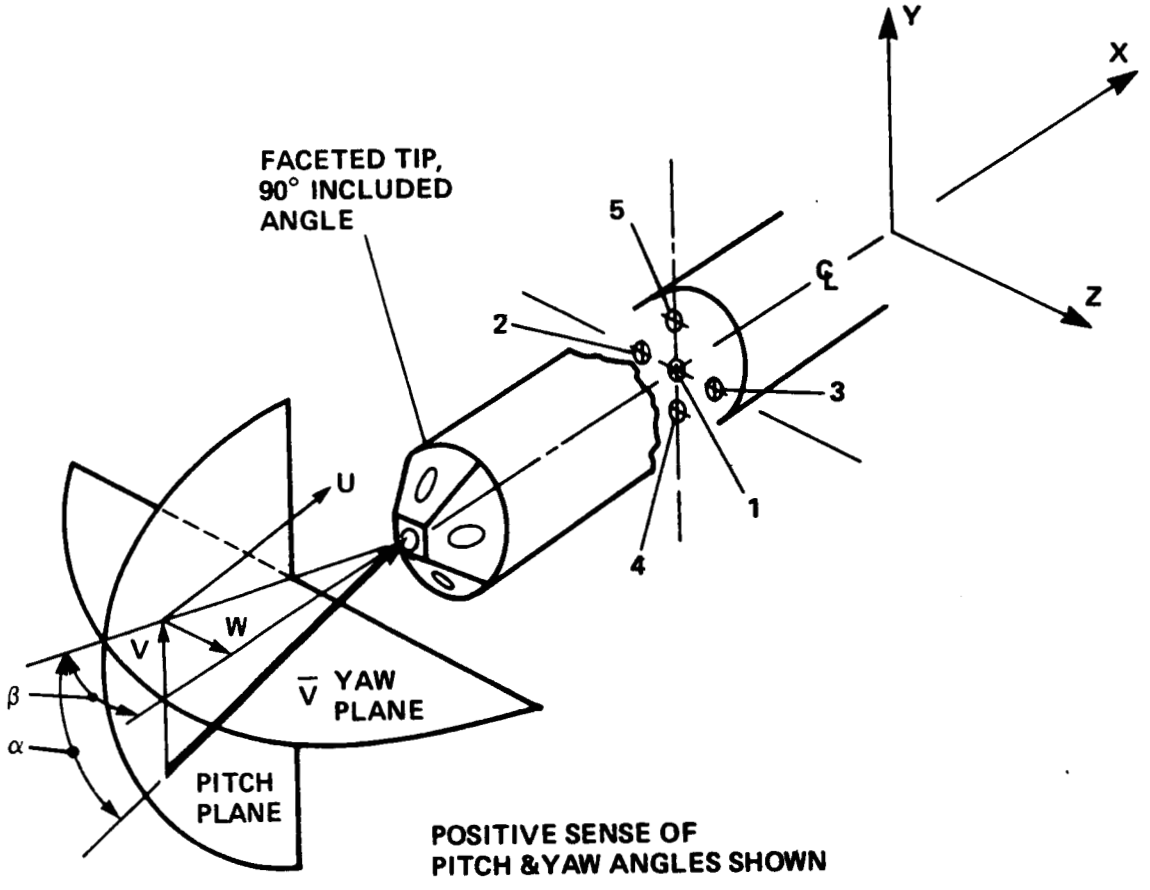

Figure 22. - Five-hole probe geometry and numbering convention.

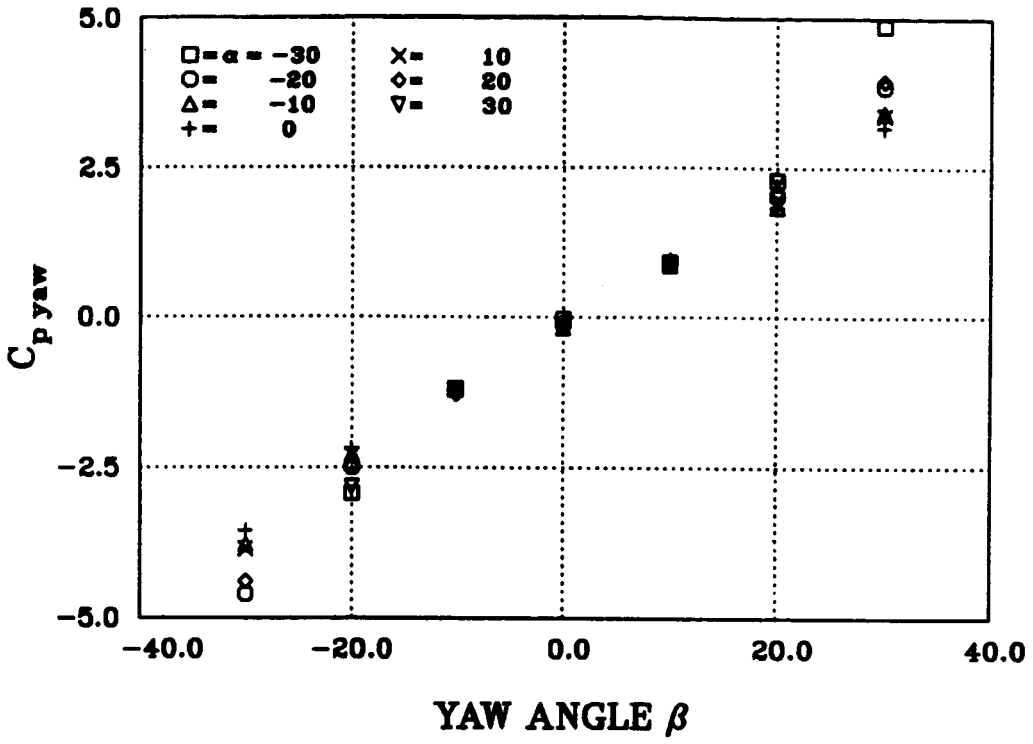

Figure 23. - $C_{P,yaw}$ vs. yaw angle β, digitized data of reference 23.

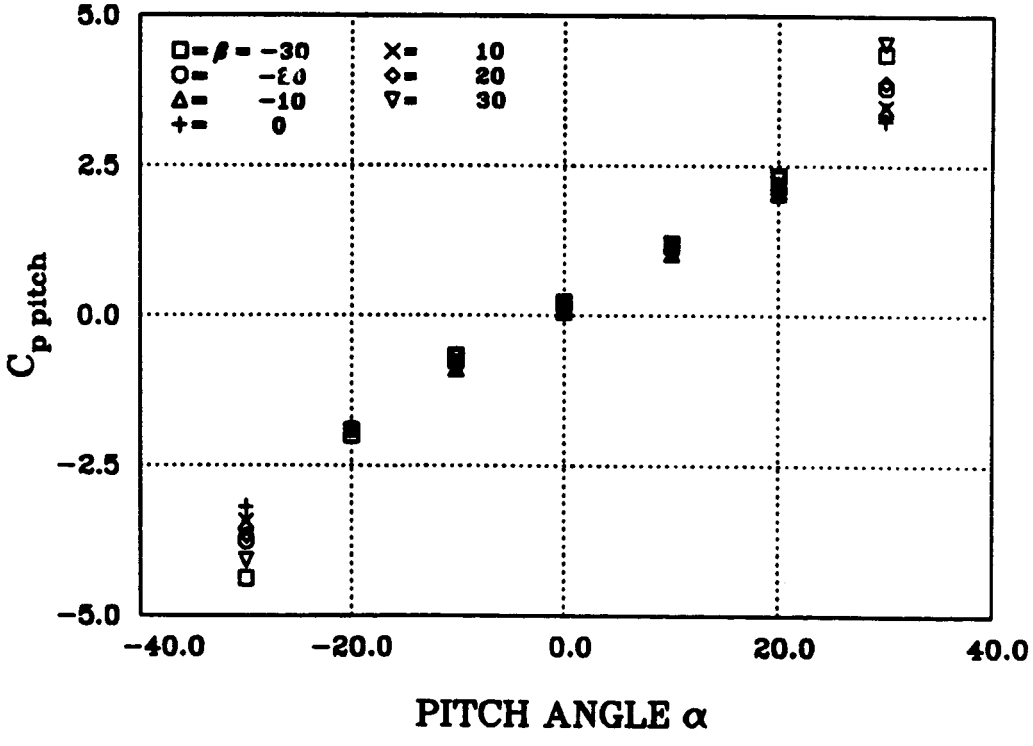

Figure 24. - $C_{P,pitch}$ vs. pitch angle α, digitized data of reference 23.

NASA National Aeronautics and Space Administration

Report Documentation Page

1. Report No.	2. Government Accession No.	3. Recipient's Catalog No.
NASA TM 88361		

4. Title and Subtitle

Interaction Between a Vortex and a Turbulent Boundary Layer
Part I: Mean Flow Evolution and Turbulence Properties

5. Report Date

January 1987

6. Performing Organization Code

7. Author(s)

Russell V. Westphal, Wayne R. Pauley and John K. Eaton (Stanford University, Stanford, CA)

8. Performing Organization Report No.

A-86408

10. Work Unit No.

505-60-31

9. Performing Organization Name and Address

Ames Research Center
Moffett Field, CA 94035

11. Contract or Grant No.

13. Type of Report and Period Covered

Technical Memorandum

12. Sponsoring Agency Name and Address

National Aeronautics and Space Administration
Washington, DC 20546

14. Sponsoring Agency Code

15. Supplementary Notes

Point of Contact: R. V. Westphal, Ames Research Center, MS 260-1, Moffett Field, CA 94035, (415)694-4140 or FTS 464-4140

16. Abstract

An experimental study was conducted to examine the interaction between a single weak streamwise vortex and a two-dimensional turbulent boundary layer. Attention was focused on characterizing the effect of the boundary layer on the vortex, including the effects of a moderate adverse pressure gradient. Rapid growth of the vortex core was observed, and a flattening of the core shape occurred when the dimension of the core radius became comparable to the distance of the vortex center from the surface. Adverse pressure gradient caused an increase in the rate of core growth, and therefore, a stronger distortion of the core shape. Measurements of surface skin friction beneath the vortex and some of the Reynolds stresses are also presented.

17. Key Words (Suggested by Author(s))	18. Distribution Statement
Vortex, Boundary layer, Turbulence, Vortex interaction, Core, Vortex generator	Unlimited - Unclassified Subject category: 34

19. Security Classif. (of this report)	20. Security Classif. (of this page)	21. No. of pages	22. Price
Unclassified	Unclassified	46	A03

For sale by the National Technical Information Service, Springfield, Virginia 22161